TU Wien

DIPLOMARBEIT

A Receiver for Optical Free Space Quantum Communication

Ausgeführt am

Atominstitut

der Technischen Universität Wien

unter der Anleitung von

o.Univ.-Prof. Dr. Anton Zeilinger

durch

Matthias Fink

December 2014

Matthias Fink

TECHNISCHE UNIVERSITÄT WIEN

Abstract

Fakultät für Physik
Atominstitut

Master of Science

A Receiver for Optical Free Space Quantum Communication

by Matthias Fink

In the last 100 years our ways of communication have changed drastically. The world turned into a village and teaming up with people around the world is a winning concept across the board. Insufficient security is a serious problem, which makes us think about new ways of encoding data. Quantum cryptography offers the opportunity to solve this problem and is therefore a main region of interest of the last decades. The main goal is, to build up a quantum network on a global scale. Therefore, a satellite space-to-ground link is indispensable. This thesis presents how to build a proper receiver for such a link.

Contents

Chapter 1

Introduction

We live in an age of digital communication. Things like mails, newspapers and even our money are just bits on any memory. Needless to say, we desperately need ways to communicate such digits securely. But commonly used cryptosystems like RSA (Rivest, Shamir und Adleman) which use asymmetric keys are not proven to be secure and rely on the *Computational Hardness Assumption*. To put it another way:

"In a society like ours, where information and secure communication are of the utmost importance, one cannot tolerate such a threat. For instance, an overnight breakthrough in mathematics could make electronic money instantly worthless." [1]

The *one-time-pad* is the only provably secure cryptosystem known today. For such symmetrical key systems one has to provide *Alice* and *Bob* (common names of the sender and receiver, respectively) with an identical key, which can be used to encrypt and decrypt a message. Doing so, we face the problem of having to share the key on an absolutely trusted path, which is where quantum physics comes in.

Additional to the classical channel, like the internet, a quantum channel can be used for key sharing. In such a quantum link, Qubit's (Section 3.3) replace classical bits. Those Qubit's can be realised with single photons. Therefore, the quantum channel is nothing more than an ordinary optical connection. In the last decade, there was a lot of research to the topic of *Quantum Key Distribution* (QKD) most of them has been using optical fibres [2] [3] [4] [5] [6]. Such fibre-based QKD-systems are well developed and already available at the market [1]. Effects like losses and decoherence in fibres restrict such systems to distances of 100-200km [7] [8] [9] [10] [11].

A major step, to extend such systems to global distances, is to achieve a quantum link to a satellite. A collaboration project between the Chinese Academy of Science, the

[1] id Quantique, http://idquantique.com; MaqiQ Technologies, http://www.magiqtech.com

University of Vienna, and the Austrian Academy of Science, with the title *Quantum Experiments at Space Scale* (QUESS), works on such a link. Within QUESS it was my task to build a proper receiver (Bob-module) for this experiment.

Therefore, I have built two receivers. One with an aperture diameter of $8mm$ and a larger one with an aperture $1''$. The $8mm$-Bob was originally designed to be attached to a camera objective. But this receiver also works with the telescope in Vienna. Measurements with this combination will be presented in Chapter 6.

Since the aperture of $8mm$ is too small for other ground stations (see Section 5.1) a second receiver was designed and built. Some tests of this module are actually running in the Laboratory and at a telescope in Graz.

This thesis is a report about the problems which occur within such a device and will present some solutions. But before that, I want to give a short overview on QUESS and the involved ground stations within this and the next Chapter.

Afterwards some basics about quantum key distribution and classical optics will be discussed in Chapter 3 and 4.

In Chapter 5 the elements of the Bob module will be presented in detail.

1.1 Quantum Experiments at Space Scale

The purpose of QUESS is to establish a quantum space to ground link for the very first time. Therefore, a Chinese satellite, equipped with photon sources, will be launched in 2015 or 2016. This satellite will be used for demonstrating quantum communication protocols and investigate fundamental questions of nature. The task of IQOQI is to provide *Optical Ground Stations* (OGS) in Europe to be utilized as a receiving station for the intended experiment.

The satellite will feature two different photon sources. One is a so called *Decoy-Source*, which emits weak laser pulses at a wavelength of $850nm$ with a repetition rate of $100MHz$ and a mean photon number of less then 1. The other source will produce entangled photon pairs at a wavelength of $810nm$. An additional Q-switch laser ($532nm$, $10kHz$) will be used for tracking and synchronisation purposes.

The satellite will be launched to a sun-synchronous orbit (Figure 1.2). This means the orbit plane rotates at the mean rate of the earth about the sun. Doing so, this satellite will be visible for any ground station every night during the year. Furthermore, the

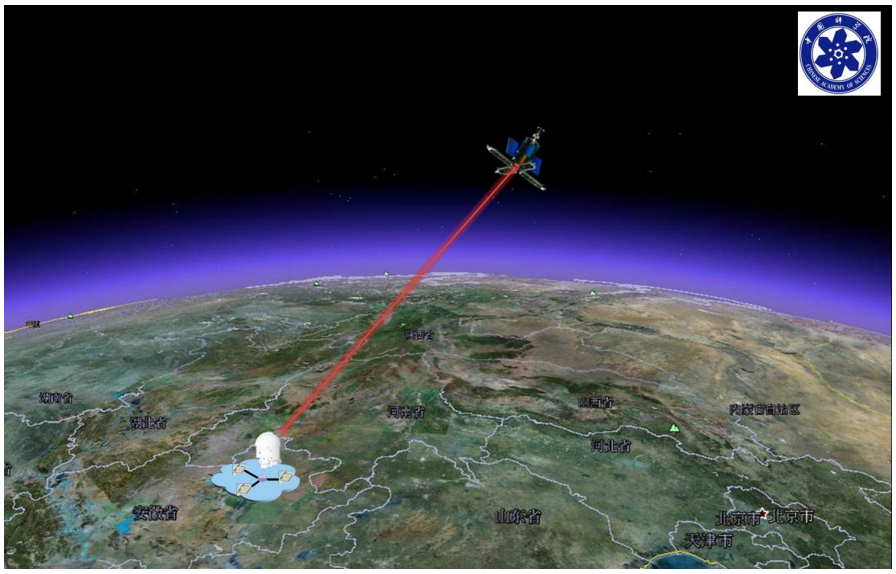

FIGURE 1.1: Satellite space to ground link. Picture by University of Science and Technology of China, CAS

local time of "day", for which the satellite will be visible, is the same in every night. Therefore, we will get comparable measurement results over the whole year.

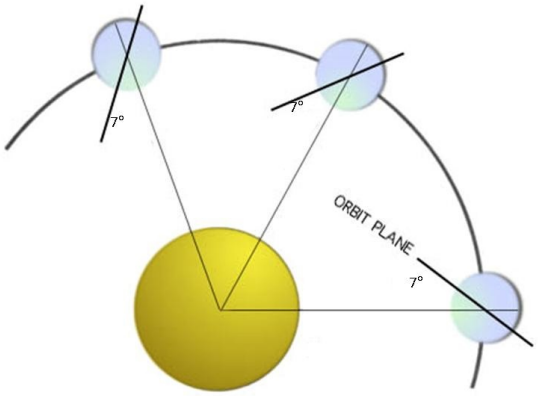

FIGURE 1.2: sun-synchronous orbit $\longrightarrow$ The orbit plane rotates at the mean rate of the earth about the sun. Picture by NASA, Landsat7 Science Data Users Handbook

The height of the satellite will be $600km$ above sea level. This results in a $90min$ Orbit and $200s$ overflight time. Thus we will be able to start measurements every $1{,}5h$ with a measurement duration which is roughly of the same order as the overpass time.

The light cones emitted by the satellite will not be collimated to the diffraction limit. The divergence angle of the quantum channel will be in the order of $15\mu rad$, resulting in a spot diameter at the receiver on the order of $20m$. This is quite big compared to the aperture of the OGS ($40cm - 1.5m$). Therefore, we expect losses at the link which will be in the order of $-40dB$. The divergence of the tracking laser will be $1mrad$, leading to

a much bigger spot size, in the order of 1,2km. Hence, it is guaranteed that the tracking laser hits the receiving aperture, given the satellite orbit accuracy of $\pm 500m$. If this is accomplished an automatic tracking system can be used to align the sender and the receiver.

Chapter 2

Telescope types and operated Ground Stations

There are several telescopes which will be adapted to collect the single photons from the satellite. The Austrian contribution to QUESS is, to equip four telescopes in Europe with the technology needed for this experiment. Of course, there will be additional telescopes in China. Within this chapter, I want to give a short summary of different types of telescopes followed by an overview of the four ground stations in Europe.

2.1 Reflecting Telescopes

2.1.1 Newton-Telescope

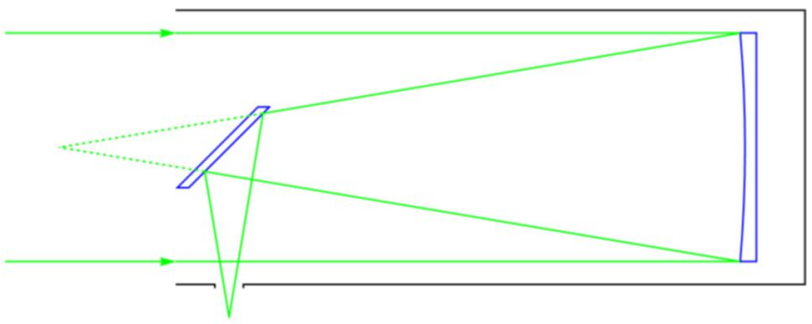

FIGURE 2.1: The Newton-Telescope consists of two mirrors (blue) and a tube (black). The trace of two incoming light-rays is shown in green.

The *Newton-Telescope* was the first working design for a reflecting telescope and was developed and built by *Isaac Newton* in 1668. It is known as the simplest design for a reflecting telescope (see Figure 2.1) and consist of a *Tube* and two mirrors. The parabolic or spherical *Primary Mirror* focuses the incoming light. The plane *Secondary Mirror* is used to reflect the light through a hole out of the tube. In that way the *Real image* in the focal plane can be easily recorded by a camera or converted to a *Virtual image* by an Eyepiece. A disadvantage of this construction is the position of the analyzing equipment which is for some applications much more then just a camera. The whole equipment has to be placed at the tube. To reduce the torque at the axes of the mount of the telescope one has to work with counter weights. In this way, the load for the mount increases rapidly with the weight of the setup.

2.1.2 Nasmyth-Telescopes

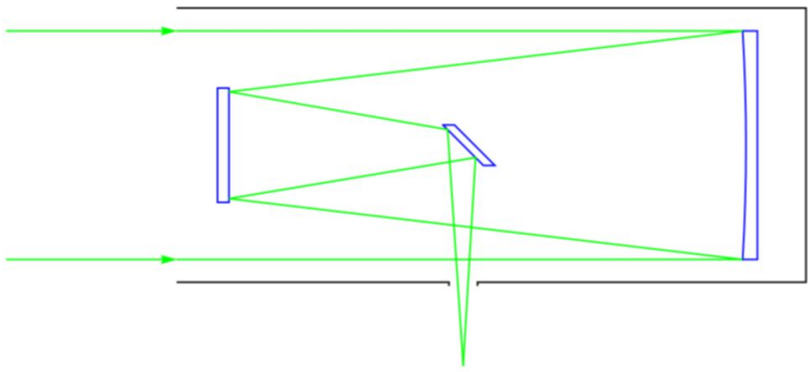

FIGURE 2.2: The Nasmyth-Telescope consists of three mirrors (blue) and a tube (black). The trace of two incoming light-rays is shown in green.

Nasmyth-Telescopes use a convex secondary mirror and an plane tertiary mirror, which is placed on the altitude axis (see Figure 2.2). The light exits the tube through a hole in the middle of the altitude bearing. An Optical set up, which can be placed behind this bearing, rotates with the telescope in the azimuth angle only. This is why this construction is commonly used for large and heavy set-ups. With additional mirrors one can guide the light through the mount of the telescope and place the focal point at a fixed position which is independent of the movement of the telescope. This focus is called *Coude focus*.

2.1.3 Cassegrain-Telescopes

Cassegrain-Telescopes consist of two mirrors. The secondary mirror is hyperbolic and reflects the light through a hole in the primary mirror (see Figure 2.3). The Cassegrain

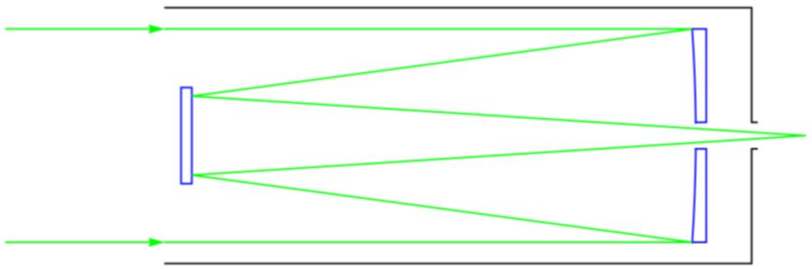

FIGURE 2.3: The Cassegrain-Telescope consists of two mirrors (blue) and a tube (black). The trace of two incoming light-rays is shown in green.

construction is often combined with a Nasmyth construction. Therefore, a removable tertiary mirror can be used to switch between those two focal planes. If one further adds the possibility to rotate the tertiary mirror by 180°, one can guide the focal point to three different positions.

2.1.4 Schiefspiegler-Telescope

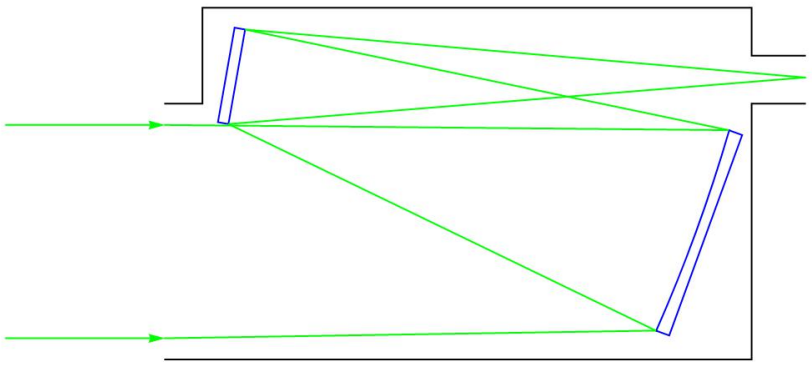

FIGURE 2.4: The Schiefspiegler-Telescope consists of two mirrors (blue) and a tube (black). The trace of two incoming light-rays is shown in green.

The benefit of the Schiefspiegler-Telescope, which works with an inclined primary mirror, is the absence of the shadow of the secondary mirror. This leads to more light in the focal plane but also to increased coma and astigmatism.

The Yolo-construction looks like a Schiefspiegler-Telescope but uses two concave mirrors with the same radius of curvature. This design eliminates coma, but leaves significant astigmatism.

2.2 Hedy Lamarr Telescope Vienna - Austria

FIGURE 2.5: Dome of the Hedy Lamarr Quantum Communication Telescope at the rooftop of IQOQI in Vienna.

The Telescope in Vienna (200m above sea level) is located at the top of our Institute (IQOQI). This telescope offers the opportunity to test the developed equipment directly next to the laboratory. Furthermore one can get an impression of how the city environment affects the quantum link.

Therefore a corner-cube-reflector was positioned, $5km$ away, at a hut in a vineyard on a hill next to Vienna (See Figure 6.5). Furthermore a sender could be placed at various distances in town, e.g. at the tower of the *Zentralanstalt für Meteorologie und Geodynamik* ZAMG which is located $3km$ away from IQOQI.

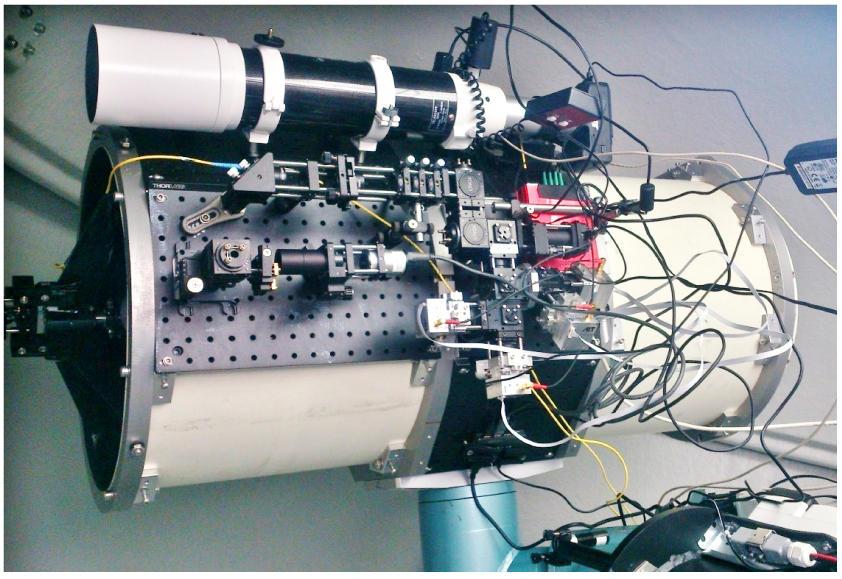

FIGURE 2.6: This Picture shows the Newton-Telescope equipped with the optical set-up for QKD and a guiding telescope (black tube).

This ground station presently consist of a *Newton-Telescope* on an *Equatorial Mount*. The size of the *Primary* and *Secondary Mirror* (PM and SM) are $40cm$ and $10cm$ in diameter, respectively. The focal length of the PM is $120cm$ while the SM is plane.

Figure 2.6 shows the telescope full equipped with the set-up which was needed for the measurement presented in Section 6.2. The EOS 500 camera, which is attached to the guiding telescope, has a large *Field of View* (FoV) of $10mrad$ and can therefore be used to find objects easily. Additional there are two small refracting telescopes attached to the main tube, with apertures of $1{,}2cm$ and $5cm$, respectively. Those refractors can be used to send light directly towards the pointing direction of the telescope. Two motorized rotation stages, equipped with a polarizer and a half wave plate, provide the possibility to alter the polarization of the $5cm$-beam.

2.3 Observatorium Lustbühel Graz - Austria

FIGURE 2.7: Cassegrain-Telescope in Graz equipped with the optical set-up for QKD. The smaler tube on the left side of the main telescope is a refracting telescope with Coude-path. Picture made by Johannes Handsteiner

The ground station in Graz is located at the Lustbühel right out of town (500m above see level). This Cassegrain-Telescope is installed on an altitude-azimuth-mount with a pointing precision below $5\mu rad$. The PM and SM with the diameters of $50cm$ and $15cm$ are slightly bigger than in Vienna. The additional refracting telescope has got an optical path (Coude-path) to a laser-room in the basement. This set-up is actually used for laser ranging purposes and works at a wavelength of $532nm$.

2.4 Cephalonia - Greece

FIGURE 2.8: OGS-Cephalonia, Picture made by Rupert Ursin and Thomas Scheidl.

The ground station in Cephalonia was specially built for QUESS. It is the largest and newest telescope of those four and is installed on an altitude-azimuth-mount. The PM and SM have a diameter of 1,4m and 36cm, respectively. The effective focal length of those mirrors is 16,8m. A flip mirror offers the possibility to either use a Cassegrain-focus or two Nasmyth-foci.

2.5 OGS Tenerife - Spain

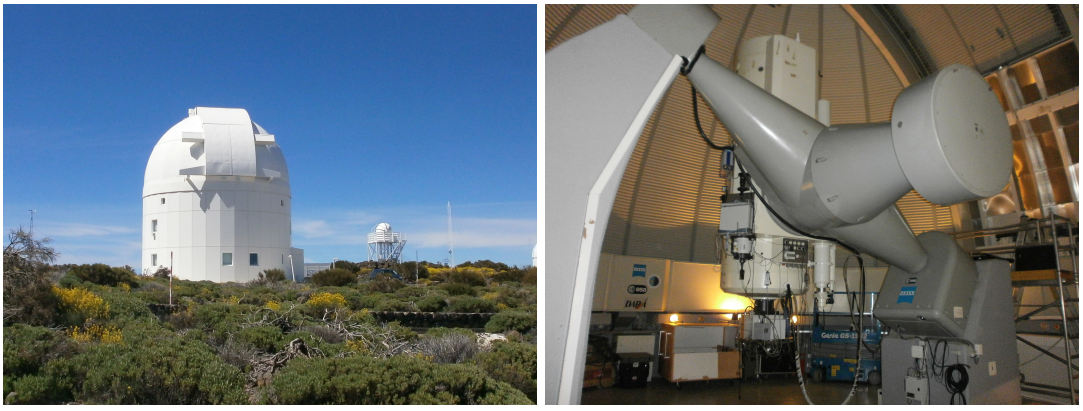

FIGURE 2.9: OGS-Tenerife

The OGS at the Teide in Tenerife is located 2400m above see level. Many quantum mechanical experiments took place on a horizontal link between the neighbouring island La Palma and Tenerife [12] [13] [14] [15]. It is installed on an equatorial-mount and offers different Cassegrain-foci (focal length 13,3m). One of those is extended with a Coude-path (focal length 38,95m). The diameter of the PM and SM are 1m and 20cm, respectively. The pointing precision while following a satellite is roughly 290μrad.

Chapter 3

Quantum Key Distribution

In this chapter, I want to discuss how Quantum Key Distribution (QKD) can be realized with polarized photons. Therefore, the first two sections show how the polarization of light can be described and manipulated. In Section 3.3 I discuss how those states can be used to form a Qubit. Entangled Qbis are of main interest in QKD so this topic will be treated in Section 3.4 and 3.5, followed by a discussion about how those Qubit's can be used for quantum cryptography and fundamental test of nature. In the end of this chapter I will show how the components needed for such experiment can be realised.

3.1 Polarisation and Jones calculus

The electric field components E_x and E_y of light, in empty space, which travels along z-direction are described classically by the Maxwell's equations. Solving those equations leads to the following expression:

$$\begin{pmatrix} E_x(t) \\ E_y(t) \end{pmatrix} = \begin{pmatrix} E_{0x} e^{i(kz-\omega t+\phi_x)} \\ E_{0y} e^{i(kz-\omega t+\phi_y)} \end{pmatrix} = E_0 \begin{pmatrix} a \\ b e^{i\varphi} \end{pmatrix} e^{i(kz-\omega t-\phi_x)} \tag{3.1}$$

with

$$\varphi = \phi_y - \phi_x, \qquad E_0 = \sqrt{E_{0x}^2 + E_{0y}^2},$$

$$a = \frac{E_{0x}}{E_0} = \sin(\gamma), \qquad b = \frac{E_{0y}}{E_0} = \cos(\gamma), \tag{3.2}$$

$$k = \frac{2\pi}{\lambda} \qquad \text{and,} \qquad \omega = ck.$$

In Equation 3.2, λ denotes the wavelength, c the speed of light , E_0 stands for the amplitude of the electric field and, φ denotes the phase difference between the x- and the y-components of the field. Furthermore, the angle γ will be referred to, within this theses, as pitch angle. The complex vector

$$\begin{pmatrix} a \\ be^{i\varphi} \end{pmatrix} = \begin{pmatrix} \sin(\gamma) \\ \cos(\gamma)\, e^{i\varphi} \end{pmatrix} \tag{3.3}$$

in Equation 3.1 is called Jones vector and describes the polarisation of the light. Without limiting the generality, we can choose the x- and y-direction as horizontal and vertical, respectively and denote the basis of this vector by

$$\begin{pmatrix} 1 \\ 0 \end{pmatrix} = |H\rangle, \ \begin{pmatrix} 0 \\ 1 \end{pmatrix} = |V\rangle \tag{3.4}$$

and decompose the vector in its *Horizontal* ($|H\rangle$) and *Vertical* ($|V\rangle$) basis-vectors:

$$\sin(\gamma)\,|H\rangle + \cos(\gamma)\, e^{i\varphi}|V\rangle. \tag{3.5}$$

I would like to note here, that the used *Bra-Ket notation* $|...\rangle$ simply indicates a vector in a Hilbert-space like $\mathbb{C}^n$, as it is common in quantum mechanics. Two different basis systems which are often used are the *Plus/Minus* 45° basis

$$\begin{aligned} |+45°\rangle &= \frac{1}{\sqrt{2}}\begin{pmatrix} 1 \\ 1 \end{pmatrix} = \frac{1}{\sqrt{2}}\left(|H\rangle + |V\rangle\right) \\ |-45°\rangle &= \frac{1}{\sqrt{2}}\begin{pmatrix} 1 \\ -1 \end{pmatrix} = \frac{1}{\sqrt{2}}\left(|H\rangle - |V\rangle\right) \end{aligned} \tag{3.6}$$

and the *Right/Left handed* circular basis

$$
\begin{aligned}
|R\rangle &= \frac{1}{\sqrt{2}}\begin{pmatrix}1\\-i\end{pmatrix} = \frac{1}{\sqrt{2}}\left(|H\rangle - i|V\rangle\right)\\
|L\rangle &= \frac{1}{\sqrt{2}}\begin{pmatrix}1\\i\end{pmatrix} = \frac{1}{\sqrt{2}}\left(|H\rangle + i|V\rangle\right)
\end{aligned}
\tag{3.7}
$$

Every state of polarization like 3.3 is represented as a point at the *Bloch sphere* (Figure 3.1). To map the Jones vector at the sphere we use the phase difference φ as an azimuthal angle and $\gamma_B = 2\,\gamma = 2\,\tan^{-1}(\frac{a}{b})$ as the polar angle.

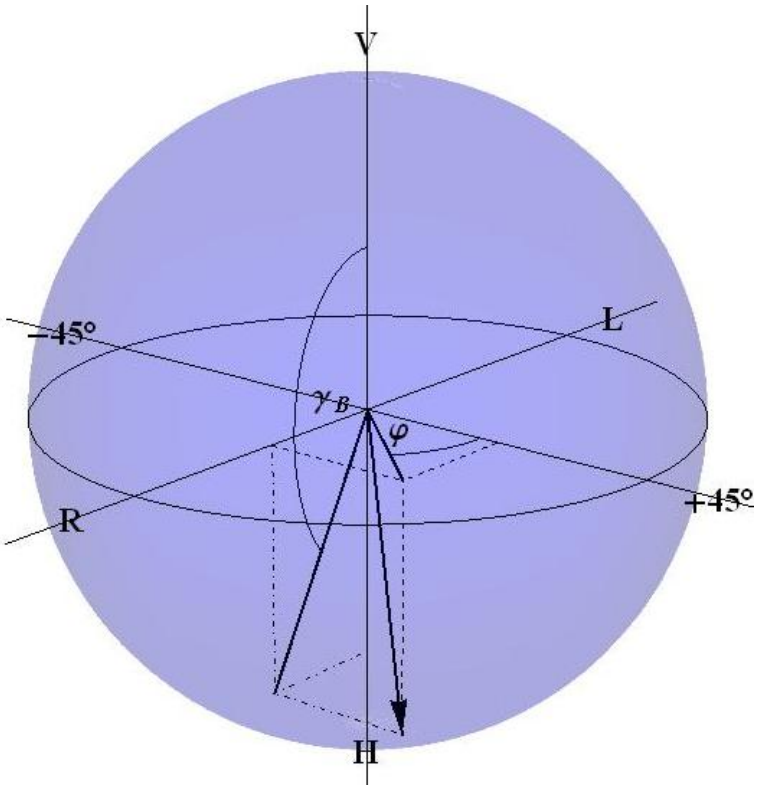

FIGURE 3.1: The black arrow indicates a specific point at the *Bloch sphere* which corresponds to a state of polarization.

3.2 Wave-Plates

One can manipulate the state of polarization of light with *Half-Wave-Plates* (HWP) and *Quarter-Wave-Plates* (QWP). These plates consist of a birefringent crystal with it's optical axis parallel to the surface of the plate. The refractive index for the components parallel to this axis differs from the refractive index for the components perpendicular

to this axis. This leads to a phase difference between those components. The thickness of a HWP is designed in a way, that the phase difference after passing through is $\frac{\lambda}{2}$. In the case of an QWP the phase difference is $\frac{\lambda}{4}$.

This manipulation can be described mathematically by the Jones matrices which act on the Jones vectors. The matrix for HWP and QWP is given by:

$$HWP(\theta) = \mathbf{R}(\theta)\, e^{i\pi/2} \begin{pmatrix} 1 & 0 \\ 0 & -i \end{pmatrix} \mathbf{R}(-\theta) = e^{-i\pi/2} \begin{pmatrix} \cos(2\,\theta) & \sin(2\,\theta) \\ \sin(2\,\theta) & -\cos(2\,\theta) \end{pmatrix} \tag{3.8}$$

$$QWP(\theta) = \mathbf{R}(\theta)\, e^{i\pi/4} \begin{pmatrix} 1 & 0 \\ 0 & -i \end{pmatrix} \mathbf{R}(-\theta) \tag{3.9}$$

The matrix

$$\mathbf{R}(\theta) = \begin{pmatrix} \cos(\theta) & -\sin(\theta) \\ \sin(\theta) & \cos(\theta) \end{pmatrix} \tag{3.10}$$

rotates the waveplate at a position where the angle θ is enclosed by the fast axis of the plate and the horizontal axis.

With a QWP and HWP combination one can reach any point at the Bloch sphere from any point of the sphere. The state of polarisation undergoes a continuous change during rotation of the plates. These changes form a path on the sphere which is shown in Figure 3.2.

3.3 Qubit

A classical *binary digit* (bit) can have the value 0 or 1. Therefore, it carries the information Yes $\mapsto$ 1 or No $\mapsto$ 0. Such a bit can be realised for example by an ordinary light bulb which can ether be On $\mapsto$ Yes $\mapsto$ 1 or Off $\mapsto$ No $\mapsto$ 0.

It's quantum mechanical equivalent is called Qubit $|Q\rangle$. Such a Qubit is a state of a quantum mechanical two-level system which can be described within a two-dimensional Hilbert-space $\mathcal{H}$. An orthonormal basis of this space is given by $|1\rangle$ and $|0\rangle$.

$$\begin{aligned} \langle 1|1\rangle &= \langle 0|0\rangle = 1 \\ \langle 1|0\rangle &= \langle 0|1\rangle = 0 \end{aligned} \tag{3.11}$$

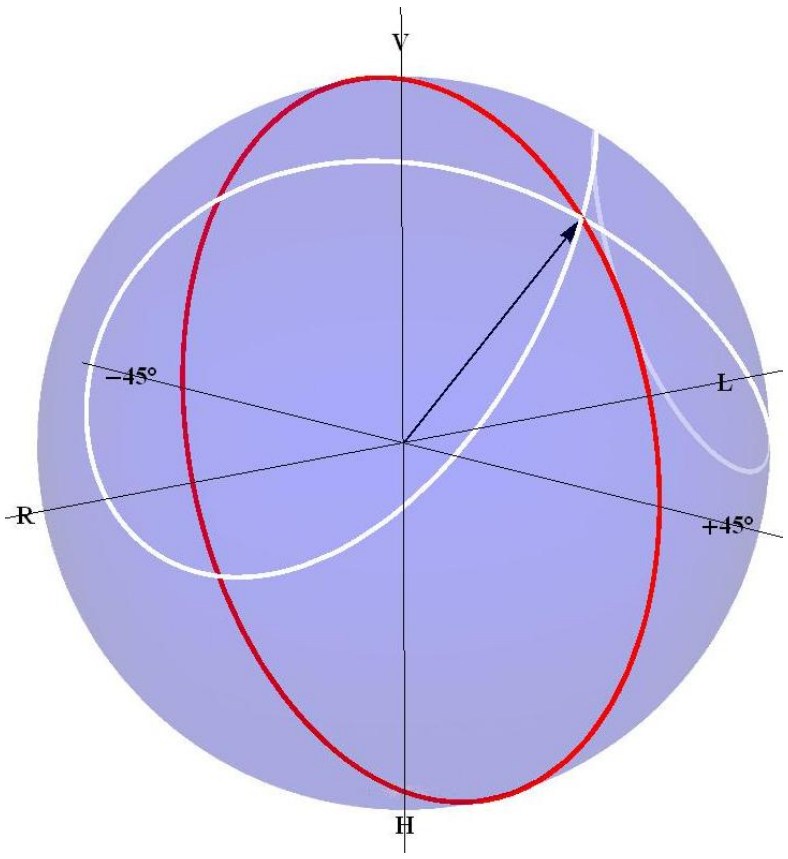

FIGURE 3.2: The black arrow indicates a state of polarisation at the Bloch sphere. This state can be manipulated with wave-plates. The rotation of such plate leads to a wander of this vector along a path at the sphere. Red ↦ Path of HWP, White ↦ Path of QWP

The general state of such Qubit can be written as a linear combination of those basis vectors.

$$|Q\rangle = A|0\rangle + B|1\rangle \quad with \quad |A|^2 + |B|^2 = 1 \quad and \quad A, B \in \mathbb{C} \tag{3.12}$$

Equation 3.12 describes a Qubit which is in a superposition of the states $|1\rangle$ and $|0\rangle$. This means the outcome of a measurement is not determined, but the probability to measure this Qubit in the state $|0\rangle$ or $|1\rangle$ is given by:

$$\begin{aligned} \langle Q||0\rangle\langle 0||Q\rangle = (\langle 0|A^*|0\rangle + \langle 1|B^*|0\rangle)\langle 0||Q\rangle = (A^*\langle 0|0\rangle)(A\langle 0|0\rangle) = |A|^2 \\ \langle Q||1\rangle\langle 1||Q\rangle = \quad ... \quad = |B|^2 \end{aligned} \tag{3.13}$$

One can see clearly the similarity between Equation 3.5 and 3.12. The reason for this is that the two orthogonal polarization states of a photon $|H\rangle$ and $|V\rangle$ are such a two-level

system and can therefore be used to realize a Qubit. If we identify $|H\rangle$ with $|0\rangle$ and $|V\rangle$ with $|1\rangle$, we can rewrite Equation 3.12 with

$$|A| = \sin(\gamma), \quad |B| = \cos(\gamma) \quad \textit{and}, \quad \varphi = \varphi_B - \varphi_A \tag{3.14}$$

to

$$|Q\rangle = |A|e^{i\varphi_a}|0\rangle + |B|e^{i\varphi_b}|1\rangle = e^{-i\varphi_a}(\sin(\gamma)|H\rangle + \cos(\gamma)e^{\varphi}|V\rangle), \tag{3.15}$$

where φ_a is a global phase of the state which is not measurable. We can further define 0 and 1 in a different basis system, by identifying $|+45°\rangle$ with $|0\rangle$ and $|-45°\rangle$ with $|1\rangle$. If we prepare a Qubit in a way that is a logical 0 in the $\pm 45°$-basis

$$|Q\rangle = |+45°\rangle = \frac{1}{\sqrt{2}}\left(|H\rangle + |V\rangle\right), \tag{3.16}$$

and perform a measurement in the H/V-basis, then we will find the photon either with the polarization H or V. Both measurement results will occur with the same probability of 50%. This means, the outcome of a logical 0 or 1 is total random if one measures in "the wrong" basis system. This behaver is of great advantage in cryptography.

3.4 Entangled State

The polarization of a single photon can be described in a two dimensional Hilbert-space $\mathcal{H}$. Therefore, a system of two photons $|...\rangle_1 \in \mathcal{H}_1$ and $|...\rangle_2 \in \mathcal{H}_2$ can be written as a tensor product of both states.

$$|...\rangle_1 \otimes |...\rangle_2 \in \mathcal{H} = \mathcal{H}_1 \otimes \mathcal{H}_2 \tag{3.17}$$

A basis of this four-dimensional Hilbert-space is given by the four *Bell states*:

$$\begin{aligned} |\Psi^{\pm}\rangle &= \frac{1}{\sqrt{2}}\left(|H\rangle_1 \otimes |V\rangle_2 \pm |V\rangle_1 \otimes |H\rangle_2\right) = \frac{1}{\sqrt{2}}\left(|H\rangle_1|V\rangle_2 \pm |V\rangle_1|H\rangle_2\right) \\ |\Phi^{\pm}\rangle &= \frac{1}{\sqrt{2}}\left(|H\rangle_1 \otimes |H\rangle_2 \pm |V\rangle_1 \otimes |V\rangle_2\right) = \frac{1}{\sqrt{2}}\left(|H\rangle_1|H\rangle_2 \pm |V\rangle_1|V\rangle_2\right) \end{aligned} \tag{3.18}$$

Those states can not be rewritten as tensor product of the basis vectors of the subsystems. Therefore we call them entangled. We can see what this means if we rewrite the rotational invariant Bell state $|\Psi^-\rangle$ in a different basis:

$$\begin{aligned}
|\theta\rangle_1 &= \cos(\theta)|H\rangle_1 + \sin(\theta)|V\rangle_1, \\
|\theta^\perp\rangle_1 &= -\sin(\theta)|H\rangle_1 + \cos(\theta)|V\rangle_1, \\
|\phi\rangle_2 &= \cos(\phi)|H\rangle_2 + \sin(\phi)|V\rangle_2 \quad \textit{and}, \\
|\phi^\perp\rangle_2 &= -\sin(\phi)|H\rangle_2 + \cos(\phi)|V\rangle_2
\end{aligned} \tag{3.19}$$

to

$$\begin{aligned}
|\Psi^-\rangle = &\frac{1}{\sqrt{2}}((\cos(\theta)\sin(\phi) - \sin(\theta)\cos(\phi))|\theta\rangle_1|\phi\rangle_2 \\
&+ (\cos(\theta)\cos(\phi) + \sin(\theta)\sin(\phi))|\theta\rangle_1|\phi^\perp\rangle_2 \\
&- (\sin(\theta)\sin(\phi) + \cos(\theta)\cos(\phi))|\theta^\perp\rangle_1|\phi\rangle_2 \\
&- (\sin(\theta)\cos(\phi) - \cos(\theta)\sin(\phi))|\theta^\perp\rangle_1|\phi^\perp\rangle_2).
\end{aligned} \tag{3.20}$$

Which reduces with $\theta = \phi$ to:

$$|\Psi^-\rangle = \frac{1}{\sqrt{2}}\left(|\theta\rangle_1|\theta^\perp\rangle_2 - |\theta^\perp\rangle_1|\theta\rangle_2\right). \tag{3.21}$$

These equations show the rotational invariance of $|\Psi^-\rangle$. Furthermore one can see that a measurement of one of those photons in any basis, which is shifted by the angle θ to the H/V-basis, results randomly in $|\theta\rangle$ or $|\theta^\perp\rangle$, each with the probability of $\frac{1}{2}$. Furthermore, a measurement of both photons (measured in the same basis $\theta = \phi$) always reveal perfect anti-correlation. Therefore, this state is called maximally entangled. The other Bell-states are also maximally entangled but not rotational invariant.

This behaviour of the photons is also observable when they are separated over great distances. The basis for the measurement can be chosen shortly before the photons are detected, such that, a communication between those photons, with speed equal or below the speed of light, can be excluded. Einstein called this property "spooky action at a distance".

3.5 CHSH inequality

The behaviour of an entangled photon pair is in contradiction with at least one of the three vital assumptions about physical theories, which have been formulated by *Einstein, Podolsky and Rosen* (EPR) in 1935 [16]:

- **completeness:** *"every element of the physical reality must have a counterpart in the physical theory."*
- **elements of reality:** *"if, without in any way disturbing a system, we can predict with certainty (i.e., probability equal to unity) the value of a physical quantity, then there exists an element of reality corresponding to this quantity."*
- **locality:** *"if two systems no longer interact, no real change can take place in the second system in consequence of anything that may be done to the first system."*

These three criteria can be used to define the class of so called *local-hidden-variable* theories. In 1964, Bell came up with an inequality which can be used to falsify local hidden variable theories [17]. *Clauser, Horne, Shimony and Holt* (CHSH) modified the Bell inequality so that it could be used in real experiments (detector efficiency below 100%, non perfect correlations)[18].

The CHSH inequality is given by:

$$-2 \leqslant C_{lhv}(\theta,\phi) + C_{lhv}(\theta',\phi) + C_{lhv}(\theta,\phi') - C_{lhv}(\theta',\phi') \leqslant +2, \tag{3.22}$$

with the correlation function

$$C(\theta,\phi) = Average[A(\theta)B(\phi)] \tag{3.23}$$

where the average is taken over a large number of experiments. The lowercase lhv indicates that this inequality is valid for local hidden variable theories. $A(\theta)$ is equal to 1 (-1) if photon 1 of the entangled pair was measured in $|\theta\rangle_1$ $(|\theta^\perp\rangle_1)$. A similar definition holds for $B(\phi)$. Therefor we can rewrite Equation 3.23 to:

$$C(\theta,\phi) = Pr(|\theta\rangle_1|\phi\rangle_2) + Pr(|\theta^\perp\rangle_1|\phi^\perp\rangle_2) - Pr(|\theta\rangle_1|\phi^\perp\rangle_2) - Pr(|\theta^\perp\rangle_1|\phi\rangle_2), \tag{3.24}$$

where $Pr()$ denotes the probability of such a measurement. If we calculate these probabilities for the polarization entangled $|\Psi^-\rangle$-state (Equation 3.20), we end up with:

$$C_{QM}(\theta, \phi) = -\cos(2(\theta - \phi)). \tag{3.25}$$

Now we can calculate the S value with the quantum mechanical correlation function C_{QM}:

$$S = C(\theta, \phi) + C(\theta', \phi) + C(\theta, \phi') - C(\theta', \phi'). \tag{3.26}$$

We find a maximum of $S = 2\sqrt{2}$ for the angles $\theta = 0$, $\theta' = \frac{\pi}{4}$, $\phi = \frac{\pi}{8}$, and $\phi' = -\frac{\pi}{8}$. This value is higher than the boundary given in Equation 3.22 and can therefore not be explained with local hidden variable theories.

The Bob-module presented in this thesis can be used to test this inequality. With the described satellite we will have the opportunity to falsify local hidden variable theories with photons which are separated on the order of $1000km$.

Since in an experiment the S value S_{exp} is reduced by experimental imperfections by $S_{exp} = S\ Vis$, with the experimentally achieved *Visibility* (Vis), a minimal Vis of $Vis_{min} = \frac{1}{\sqrt{2}}$ is required for a conclusive Bell-test.

3.6 BB84 protocol

Charles H.Bennet and Gilles Brassard proposed in 1984 the first quantum cryptography protocol which is called BB84. This protocol uses four different states like $|H\rangle$, $|V\rangle$, $|+45°\rangle$ and, $|-45°\rangle$. Two of them ($|H\rangle$ and $+45°$) are associated with logical 0 and two of them ($|V\rangle$ and $-45°$) with 1. Here it should be noted that any pair of vectors, one from each basis, have the same overlap, e.g.,$|\langle H| - 45°\rangle|^2 = \frac{1}{2}$. Hence, these bases are called mutually unbiased.

In step one Alice sends (and records) a random series of those states to Bob via the quantum channel. Bob measures the incoming photons randomly in one of the two basis systems. During this process it should be guaranteed that the sender and the receiver are able to make a one-to-one correspondence between the transmitted and the received state. Doing so both get a binary string called the *raw key*. Those strings show the same value at each position for which Alice and Bob have used the same basis.

In a second step Alice and Bob communicate to each other in which basis they have measured which state. The channel used for this communication must not be trusted since the measurement basis without result carries no information. Now both parties know in which cases they have chosen the same basis and can therefore delete all other values in the raw key. The result is called *sifted key*. In this step called basis reconciliation they have lost 50% of their key but therefore they get (in this idealistic picture) perfect identical keys.

We can think of an eavesdropper (Eve) which could branch some photons off the quantum channel. Eve could perform a measurement with those photons, but therefore they will never arrive at Bob. This means those photons will not contribute to the key and therefore Eve gains no information about the key. The only result of such an attack would be a shorter raw key.

In more advanced attacks Eve has to send a photon to Bob, for each photon she intercepts from Alice. It would be perfect for Eve to have a device which could make a copy of those photons. But such quantum copy machines are, due to the *No-cloning theorem*, even in theory imperfect (fidelity $< \frac{5}{6}$). Therefore, Eve's intervention would introduce an error to the sifted key called *Quantum bit Error Ratio* (QBER). This error can not be distinguished from a QBER caused by technical imperfections.

One can use any error correction protocol to determinate the QBER and correct those errors. Since every mismatch in the sifted key has to be assigned to be a result of Eve's intervention, one can calculate the information which Eve could possibly have. With this knowledge one can reduce Eve's information on the final key by a process called *privacy-amplification*. Since all those steps reduce the length of the key, it is of great interest to keep the QBER caused by technical imperfection as small as possible. Moreover, if the QBER reaches a value of $\approx 11\%$ no secure key can be distilled anymore, defining the limit for experimental errors.

3.7 Alice and Bob

In this Section I want to give an idea about how Alice and Bob can be realized in Experiments. In Section 3.7.1.1 a Decoy-Source is described. Section 3.7.1.2 is about a *Beam-Splitter* Source of entangled photons, which my co-worker Johannes Handsteiner developed. Finally Section 3.7.2 deals with the function principle of the Bob Modules which will be discussed in further chapters in detail.

3.7.1 Alice

3.7.1.1 Decoy-Source

A *Decoy-Source* is a variation of a *Faint-laser-pulse Source* and therefore one possibility to realise Alice. Laser pulses from a standard semiconductor laser are split into four different paths. Each of those paths emits one of the four polarizations used for BB84, e.g., Path1 $\mapsto |V\rangle$. Afterwards those paths are combined again and sent to Bob.

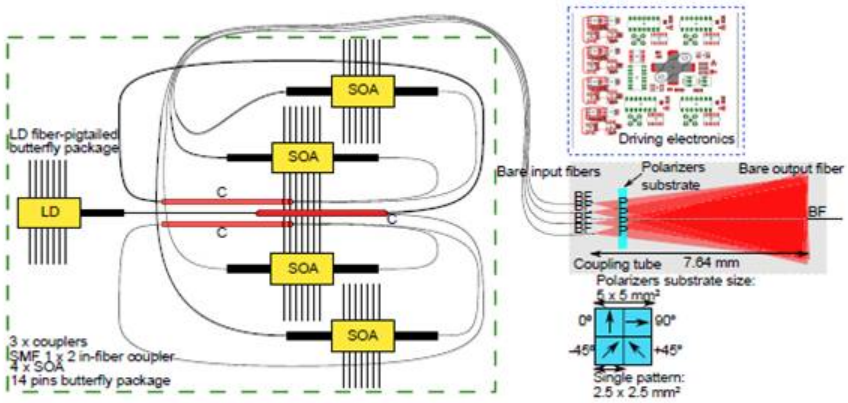

FIGURE 3.3: Schematic of a fiber based decoy-source [19]. The pulsed light of a *Laser Diode* (LD) is spitted via C (in-fiber beam splitter) into four single-mode fibers. The intensity in each fiber can be controlled via a *Semiconductor Optical Amplifier* (SOA).

The emitted laser pulses are attenuated in such way, that the result is an approximate single photon *Fock* state. The probability of finding n photons in such pulse is given by

$$P(n,\mu) = \frac{\mu^n}{n!} e^{-\mu}, \tag{3.27}$$

where μ is the mean photon number. There is always a probability for finding more than one photon in a pulse:

$$\frac{1 - P(0,\mu) - P(1,\mu)}{1 - P(0,\mu)} \simeq \frac{\mu}{2}. \tag{3.28}$$

These pulses with more than one photons can be used by Eve, which could split off one of those photons with a beam splitter.This scenario is called a *Photon Number Splitting attack* (PNS). Since the probability for such pulses is proportional to μ, one has to keep this value small ($\mu \simeq 0{,}1$). Therefore most of the pulses are empty $P(n=0,\mu) = e^{-\mu} \simeq 1 - \mu$.

One solution to this problem is the *decoy state protocol*, where Alice randomly switches between signal pulses with μ_{sig} and decoy pulses with $\mu_{dec} < \mu_{sig}$. Doing so, PNS attacks

can be detected, since it introduces different loss for the signal and the decoy pulses. Such a source will be implemented at the satellite with $\mu_{sig} = 0{,}7$ and $\mu_{dec} = 0{,}5$.

3.7.1.2 Beam-splitter Source

It is currently not specified which kind of entangled-photon source will be installed at the satellite. But my co-worker Johannes Handsteiner developed a very small and portable Beam-splitter source. This source can be used to test the ground stations, before the final experiment with the satellite. A schematic drawing of this source is shown in Figure 3.4.

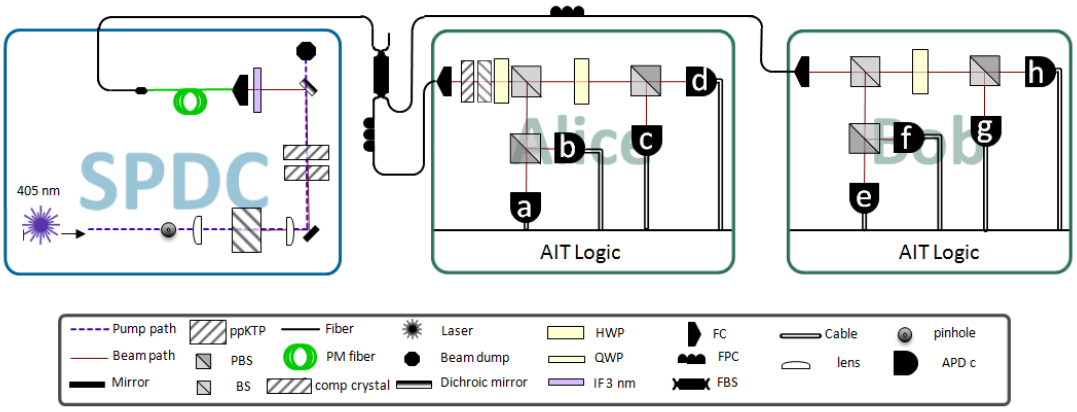

FIGURE 3.4: This Figure shows a schematic drawing of the beam-splitter source (left), Alice (middle) and, Bob (right). Picture made by Johannes Handsteiner

A $405nm$ pump-laser gets focussed in a *periodical poled Potassium Titanyl Phosphate* (ppKTP) crystal. This crystal creates out of the $405nm$ photons ,via *Spontaneous Parametric Down Conversion* (SPDC), photon pairs at $810nm$, with one $|H\rangle$ and one $|V\rangle$ polarized photon. These photons are produced simultaneously, but, due to the birefringence of the crystal, they leave the crystal with a temporal walk off. This walk off needs to be corrected with birefringent elements like compensator crystals and the *Polarisation Maintaining* (PM) fibre. A dichroic mirror and a $3nm$ interference filter are used to block out the rest of the pump-photons. Afterwards those pairs of photons are coupled into the PM fibre. This fibre offers the possibility to connect the source to a moveable telescope without altering the polarization.

At a 50 : 50 *in-fiber Beam Splitter* (FBS) each photon of a pair gets either reflected or transmitted. Doing so 50% of the pairs will split up and form a pair of entangled photons. In Figure 3.4 the two outputs of the FBS are connected to two polarization analyzing modules (Alice and Bob).

With two birefringent crystals at Alice one can manipulate the phase between the photons of one pair and produce a $|\Psi^-\rangle$-state. Therefore, Alice and Bob will get anti-correlated measurement results if they use the same basis.

3.7.1.3 Transmitting Telescope

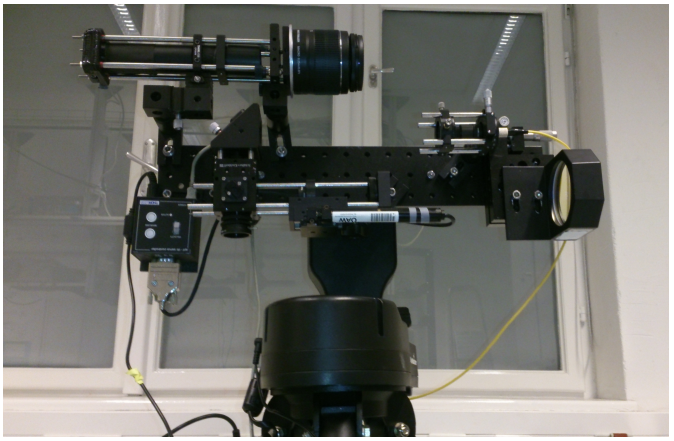

FIGURE 3.5: This picture shows the telescope which will be used to transmit the photons to the ground station.

The PM fibre from the beam-splitter source can be attached to a sending telescope (See Figure 3.5). A lens with a focal length of $2cm$ is used to collimate the divergent light from the PM fibre (core diameter $3{,}5\mu m$, numerical aperture $0{,}12rad$), leading to a beam diameter of $4{,}8mm$. This collimated light is directed to a $50:50$ beam splitter, which replaces the FBS of Figure 3.4. Therefore, this set-up contains no single-mode fibers which alter the polarization. The transmitted photons will be detected by Alice, while the reflected photons will be sent through a refractive telescope to a OGS. This refractive telescope consists of two lenses with the focus lengths of $2cm$ and $28cm$, respectively. Thus, we have a beam diameter of $6{,}7cm$ at the last lens, corresponding to a minimum divergence of the emitted light of $10\mu rad$.

The whole set-up is placed on a motorized altitude-azimuth tripod which can be controlled by a *Personal Computer* (PC). An additional camera on this tripod will be used to detect a tracking laser sent by the OGS. Therefore, a LabView computer program can be used to correct automatically the sending direction.

3.7.2 Bob

The working principle of a receiver is quite simple. A *50:50 Beam-Splitter cube* (BS) either transmits an incoming photon to the measurement in *Basis 1* (B_1) or reflects it to *Basis 2* (B_2), both with the probability of $\frac{1}{2}$. In each of these arms a *Polarizing Beam*

Splitter (PBS) transmits the *Horizontal polarized photons* (H) and reflects the *Vertical polarized photons* (V) onto a *Lens* (L) which focuses the light on a *Detector* (Det). All four detectors are fed into a coincidence logic (AIT TTM8000) which is connected to a PC. Therefore, the polarization and the arrival time of every photon can be stored on a hard disc.

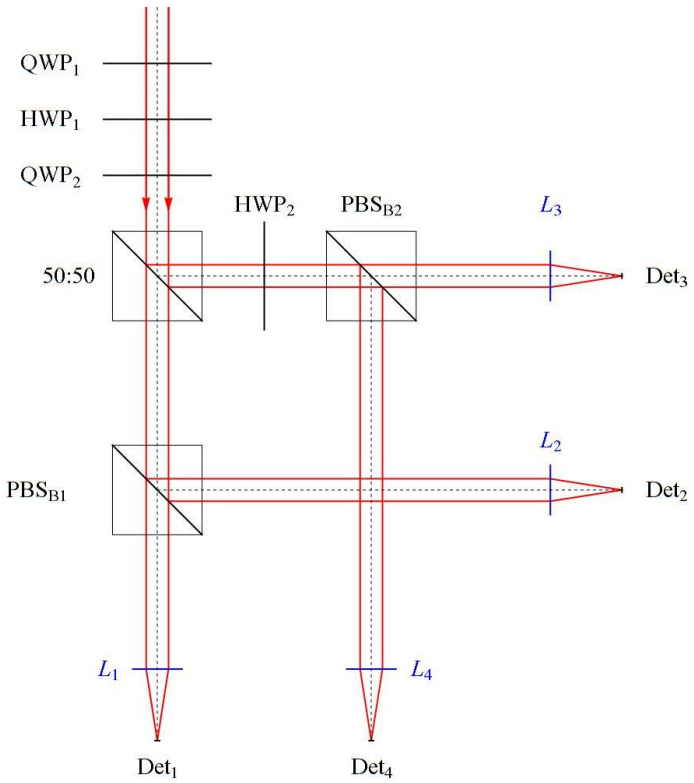

FIGURE 3.6: Arrangement of the optical elements in the 1″-receiver.

The polarization dependent separation at the PBS only works for H- and V-polarized photons. Therefore, we have to compensate possible polarization miss matches between Alice and Bob. This can be achieved with the QWP, HWP and, QWP combination in front of the BS.

A further $HWP(\frac{\pi}{8})$ (See Equation 3.8) in the reflected arm of the BS is used to convert incoming photons in the following way:

$$\begin{aligned} HWP\left(\frac{\pi}{8}\right)|H\rangle &\mapsto |+45^\circ\rangle \\ HWP\left(\frac{\pi}{8}\right)|V\rangle &\mapsto |-45^\circ\rangle \\ HWP\left(\frac{\pi}{8}\right)|+45^\circ\rangle &\mapsto |H\rangle \\ HWP\left(\frac{\pi}{8}\right)|-45^\circ\rangle &\mapsto |V\rangle. \end{aligned} \tag{3.29}$$

Therefore every incoming $|+45°\rangle$ photon which gets reflected at the BS ends up at the Det_3, while all $|-45°\rangle$ photons end up at Det_4. Incoming $|H\rangle$ and $|V\rangle$ states lead to random counts in this basis (B_2).

Figure 3.6 shows the arrangement of the optical elements in the receiver with the large aperture while Figure 3.7 belongs to the small aperture module. The main difference is the flipped over PBS in basis 1. The advantage of this arrangement is a shorter distance between the PBS and the detector in each reflected arm. Some PBS don't work ideally under exactly 45° reflection (see Section 5.2.2) and therefore have to be slightly tilted. To hit the lens in front of the detector as close as possible to the centre one has to keep the reflected arm as short as possible.

A further difference between those set-ups which is not drawn in Figure 3.7 is a rotation of the whole cage system in the B_2 arm. This rotation of 45° of the PBS_{B2} along the beam axis does not require HWP_2. Since the performance of this wave-plate is dependent on the wavelength of the light, the set-up without HWP_2 works for a bigger spectral range. The other wave-plates can be exchanged easily, without disassembling the whole set-up.

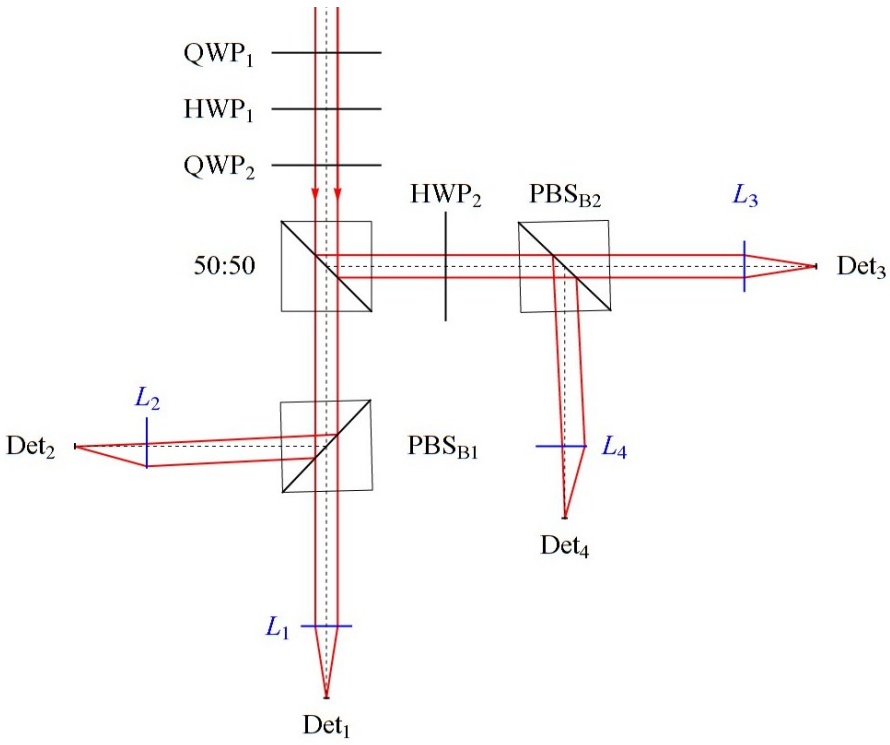

FIGURE 3.7: Arrangement of the optical elements in the $8mm$-receiver.

3.7.2.1 Coincidence Detection

Every time a photon hits a detector, this detector will produce, with a certain probability η, an electrical rectangular pulse, where η denotes the detector efficiency. The time span between the arrival time of the photon and the rising edge of the pulse is Gaussian distributed and its standard deviation σ is called jitter. The detector jitter, of the used detectors, is in the order of $1ns$.

The rectangular signal is fed to one of the 8 inputs of the coincidence logic (AIT TTM8000), which records the time of each rising edge with respect to an internal clock. The time resolution of this system is $82ps$ which is negligibly small compared to detector jitter. The time stamps of all events in each input are sent via a Gbit-Ethernet connection to a PC and stored on a hard disk. Out of this data one can generate files which consist of the time stamps, the basis and the result of each measurement.

Alice and Bob share their files without the measurement results. By comparing the measurements of Alice and Bob, which were made in the same basis, one can find time stamps differing less than a defined coincidence time window τ.

To find the right time delay between Alice and Bob one has to add different Δt to the time stamps of Bob and repeat for each value the coincidence search. Doing so, one can find a maximum of the resulting function $N_c(\Delta t)$ at the correct time delay Δt_{max}. This maximum results from the simultaneously produced photon pairs at the source, where Δt_{max} considers the difference in there optical path.

Counting those coincidences, without considering a time delay Δt between Alice and Bob, results most probably to a number N_c close to

$$N_{acc} = R_A \, R_B \, \tau \tag{3.30}$$

which is the number of expected accidental coincidences within a certain time window t. The number of detected single events, in the considered basis and time window, of Alice and Bob are denoted by R_A and R_B, respectively.

3.8 QBER

The expected $QBER_{tech}$ caused by technical imperfection can be calculated by [1] :

$$QBER_{tech} = QBER_{opt} + QBER_{det} + QBER_{acc}. \tag{3.31}$$

$QBER_{opt}$ is caused by imperfections in the optical path and is equal to the probability p_{opt} of photons going to the wrong detector

$$QBER_{opt} = p_{opt} \simeq \frac{1 - Vis_{opt}}{2}. \tag{3.32}$$

where Vis_{opt} denotes the *polarization Visibility.*

$QBER_{det}$ arises from counts of the detector caused by background light or dark counts.

$$QBER_{det} = \frac{p_{dark}\ n}{t_{link}\ \eta\ 2\ \mu} \tag{3.33}$$

The probability of registering a dark count within the expected time window at a single photon detector, is denoted by p_{dark} and the link attenuation is denoted by t_{link}. Furthermore, n is the number of detectors used and η is the detector efficiency.

For an entangled photon source, there exists a further source introducing errors. This is higher order emission at the source, i.e. the emission of two photon pairs within coherence time window. If two pohotons are detected in coincidence which do not belong to the same pair, this is called an accidental coincidence and introduces an error $QBER_{acc}$ since those two photons are not entangled. This $QBER_{acc}$ can be calculated by:

$$QBER_{acc} = \frac{p_{acc}}{2\ \mu}, \tag{3.34}$$

where p_{acc} is the probability of finding a second pair within the time window, knowing a first one was created. This probability depends on the characteristics of the source at the satellite which are not specified by now.

Chapter 4

Theoretical Background of Optics

Within this chapter, I want to present some calculations which are useful for implementing a receiver at a telescope. Furthermore, one should take care of these results when designing a receiver.

4.1 Airy Disk

The light of a star is in good approximation a plane wave front. Collecting this light with a lens, will not lead to an infinitely small spot in the focal plane. Due to the finite size of the lens/mirror which diffracts the light we will end up with an area containing the intensity of the light. Therefore, the resolution of a telescope is restricted even without atmospheric turbulence.

The resulting Intensity distribution $I(r, \phi)$ in the focal plain is rotational symmetric and given by [20]:

$$I(r, \phi) = I_0 \left(\frac{2J_1(\frac{\pi r D}{\lambda f})}{\frac{\pi r D}{\lambda f}} \right)^2 . \tag{4.1}$$

Where I_0 denotes the Intensity at $r = 0$, λ is the wavelength of the incident light, $J_1(x)$ is a Bessel functions of the first kind and, f and D are the focal length and diameter of the lens/mirror, respectively. This intensity distribution is called *Airy pattern* and the region within the first zero of the function is called *Airy disk*. The radial-distance between the central intensity maximum and the first zero is given by:

$$r_{Ad} = 1{,}22 \times \frac{f\lambda}{D}. \tag{4.2}$$

The *Full With Half Maximum (FWHM)* diameter of the Airy disk is given by

$$d_{FWHM} = 0{,}5145 \times 2 \times \frac{f\lambda}{D} = 0{,}844 \times r_{Ad} \simeq \frac{f\lambda}{D}. \tag{4.3}$$

If a second light source with an angular distance of θ to the first illuminates the lens and it's intensity maximum gets closer than r_{Ad} the two spots can no longer be differentiated. The corresponding angle

$$\sin(\theta) = 1{,}22 \times \frac{\lambda}{D}. \tag{4.4}$$

is known as the resolution of an ideal telescope.

4.2 Atmospheric turbulence and Fried parameter

The main differences between the experiments in the laboratory and space scale experiments are the grater distance and the atmospheric distortion of the beam. The latter will be examined in this section.

Fluid dynamics differ between laminar and turbulent flow. The laminar flow is associated with a layer structure and therefore a continuous velocity field. The layer structure breaks up at higher velocity and turbulent sub-flows called *eddies* appear. The Atmosphere is a highly turbulent medium and its motion is described by the Navier-Stokes equations. Because of mathematical difficulties in solving these equations, Kolmogorov developed a statistical approach of turbulence [21]. Kolmogorov theory describes these eddies from a macro-scale L_0 (outer scale of turbulence) to a micro-scale l_0 (inner scale of turbulence). The velocity of the air is related to its temperature and therefore to the refractive index n. Detailed Information on how these effects disturb a Laser beam can be found in [22]. Fluctuations of n results in a wandering and spreading of the beam. The eddies with a large diameter compared to the beam cause a beam deflection and the smaller eddies lead to phase front distortion and spreading of the beam.

Within this thesis the diameter of the laser beam at the receiver is always larger than the mirror of the telescope. Focusing some light of such a beam with a lens or a mirror to a camera leads to a bigger point size than calculated in section 4.1. The wandering of large eddies through the beam cause a *jitter* of the spot which can be resolved by camera exposure times $t_{exp} < \frac{D}{v_\perp}$, where $v_\perp$ is the mean wind speed perpendicular to the propagation path. Because of phase front distortion also pictures with short exposure times show a bigger spot than predicted in section 4.1.

These problems are well known in connection with astronomical imaging. To quantify this phenomena D.L. Fried introduced a parameter [23] which is linked to Kolmogorov theory by:

$$r_0 = 2{,}1 \times \rho_{pl} = \left(0{,}423k^2 \int_{Path} C_n^2(s)\, ds\right)^{-3/5}. \tag{4.5}$$

The *fried parameter* r_0 is proportional to the *transversal coherence radius* ρ_{pl} of a plane wave disturbed by atmospheric turbulence. The wavenumber k is given by $k = \frac{2\pi}{\lambda}$ and C_n^2 ist the refractive-index structure parameter.

The *seeing angle* β can be calculated out of the $FWHM$ diameter d'_{FWHM} of the image (i.e. the *Point Spread Function*) in the focal plane of a lens, with focal length f, by $\beta = \tan\left(\frac{d'_{FWHM}}{f}\right)$. Further, β is linked to r_0 by

$$\beta \sim \frac{\lambda}{r_0}. \tag{4.6}$$

By comparing 4.3 with 4.6 one can see clearly how atmospheric turbulence degrade the resolution of telescopes. Typically values for r_0 range, at sea level, from $2cm$ to $15cm$ for visible and infrared wavelength. Measurements of r_0 for an inter-island link between Tenerife and La Palma ($144km$) result in a range from 1cm to 5cm [24] for $\lambda = 850nm$, which corresponds to a value of $\beta = 85...17\mu rad$.

The optical-dense atmosphere around the earth is roughly $20km$ thick [25]. Therefore the expected seeing angle of a satellite-to-ground link is comparable to a horizontal link with a distance of $20km$, if the satellite is close to the zenith. The path trough the atmosphere can reach values like the one of the inter-island link, if the satellite is close to the horizon. For such constellations we expect β to be in the same magnitude like measured between Tenerife and La Palma.

4.3 Ray transfer matrix analysis

Ray transfer matrix analysis is a common way to design optical systems. This method delivers descriptive results if the traced rays satisfy the *paraxial approximation*.

We choose the coordinate system in such a way that the z-axis coincides with the *optical axis* of the components. A light ray is defined by:

$$\vec{r} = \begin{pmatrix} r \\ \alpha \end{pmatrix}, \tag{4.7}$$

where r and α denotes distance and the angle between the ray and the z-axis, respectively. Matrices which act on this vector, transfer the ray from an input plane to the output plane. The optical elements on the path between those planes are represented by Matrices (see Equation 4.9) which can be combined via multiplication.

$$T(d) = \begin{pmatrix} 1 & d \\ 0 & 1 \end{pmatrix}, \tag{4.8}$$

$$L(f) = \begin{pmatrix} 1 & 0 \\ \frac{-1}{f} & 1 \end{pmatrix} \tag{4.9}$$

The translation matrix $T(d)$ transfers the ray over a distance d on the z-axis with no elements in between. A thin lens is a good approximation, if the thickness of the lens at the optical axis is small compared to the radius of curvature of its surface. The matrix for this approximation is given in Equation 4.9 where f stands for the focal length of the Lens.

With these matrices one can calculate the vector $\vec{r}_{l1}$ in the focal plane of a thin lens by:

$$\begin{aligned} \vec{r}_{l1}(r, \alpha, f_1) &= T(f_1) \times L(f_1) \times \vec{r}(r, \alpha) \\ &= \begin{pmatrix} 1 & f_1 \\ 0 & 1 \end{pmatrix} \times \begin{pmatrix} 1 & 0 \\ \frac{-1}{f_1} & 1 \end{pmatrix} \times \begin{pmatrix} r \\ \alpha \end{pmatrix} = \begin{pmatrix} \alpha f_1 \\ \alpha - \frac{r}{f_1} \end{pmatrix}, \end{aligned} \tag{4.10}$$

where α and r denotes the ray parameters at the position of the lens.

Now we put a Camera or a Detector with diameter d_{det} in the focal plane, and calculate the *Angle of Arrival* (AoA) α_e of a plane wave, which hits the device on its edge. The *Field of View* (FoV) is given by twice this angle and results for this optical system to:

$$FoV = 2\alpha_e = 2\frac{d_{det}/2}{f_1} = \frac{d_{det}}{f_1} \tag{4.11}$$

Instead of the camera, a second lens (L_2), at the distance $f_1 + f_2$ from the first lens (L_1), can be used to collimate the light from an incident plane wave. The resulting beam at the distance z_2 is given by:

$$\begin{aligned}\vec{r}_{l2} &= T(z_2) \times L(f_2) \times T(f_1 + f_2) \times L(f_1) \times \vec{r}(r, \alpha) \\ &= \begin{pmatrix} r_{l2} \\ \alpha_{l2} \end{pmatrix} = \begin{pmatrix} \alpha \left(f_1 + f_2 - \frac{f_1}{f_2} z_2 \right) - \frac{f_2}{f_1} r \\ \alpha \frac{f_1}{f_2} \end{pmatrix}\end{aligned} \tag{4.12}$$

In Equation 4.12 and Figure 4.1 one can see clearly how these two lenses reduce ($f_1 > f_2$) or enlarge ($f_1 < f_2$) the beam radius by a factor of $V = f_2/f_1$. While the radius gets reduced, the angle between the beam and the z-axis increases by

$$\alpha_{l2} = -\frac{\alpha}{V}. \tag{4.13}$$

Furthermore there exists a plane called *Pupil Plane* in which the position of the beam is independent of α. The distance between this plane and L_2 is given by:

$$z_{pup} - z_{L_2} = f_2 \left(1 + V\right). \tag{4.14}$$

Placing a tip–tilt mirror at this position offers the possibility to correct pointing errors without beam displacement.

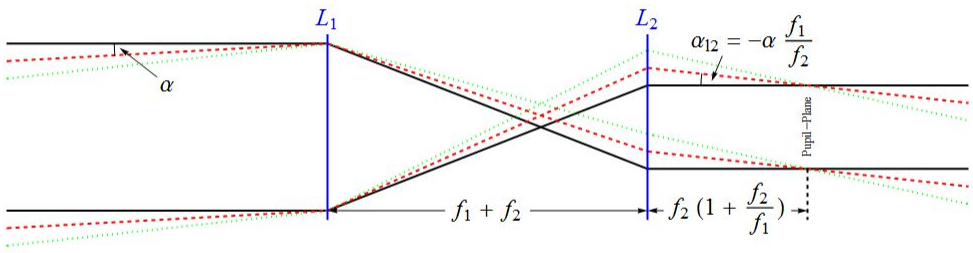

FIGURE 4.1: This Figure shows the angle amplification of a two lens system and the pupil plane.

A Detector in the focal plane of a third Lens (L_3) would have an FoV of:

$$FoV = d_{det} \frac{V}{f_3} \tag{4.15}$$

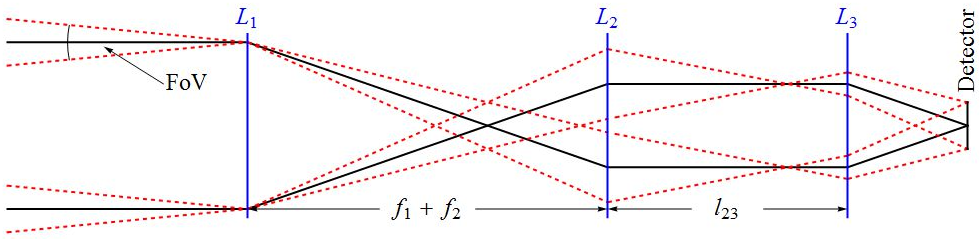

FIGURE 4.2: This Figure shows the field of view of a detector in a two lens system.

One can further define an *Effective focal length* (Efl) for a two lens system with the distance z_{12} by solving the Equation

$$\begin{pmatrix} 0 \\ 1 \end{pmatrix}^T \times \mathbf{T}(z_{diff}) \times \mathbf{L}(Efl) \times \begin{pmatrix} r \\ \alpha \end{pmatrix} = \begin{pmatrix} 0 \\ 1 \end{pmatrix}^T \times \mathbf{L}(f_2) \times \mathbf{T}(z_{12}) \times \mathbf{L}(f_1) \times \begin{pmatrix} r \\ \alpha \end{pmatrix} \quad (4.16)$$

Doing so one gets the result:

$$Efl = \frac{f_1\ f_2}{f_1 + f_2 - z_{12}}. \quad (4.17)$$

The distance of the focal plane and the second lens is given by:

$$d_{foc} = \frac{f_1\ (f_2 - z_{12})}{f_1 + f_2 - z_{12}}. \quad (4.18)$$

Figure 4.3 illustrates these calculations with an incoming beam radius of $1cm$ and two lenses with $f_1 = 5cm$ and $f_2 = -5cm$ with a distance of $z_{12} = 2cm$. The red lines show the path of the light. If one would place, instead of the red lens system, a lens with a focal length of $Efl = 12{,}5cm$, the resulting beam (blue) at the focal plane would be unchanged.

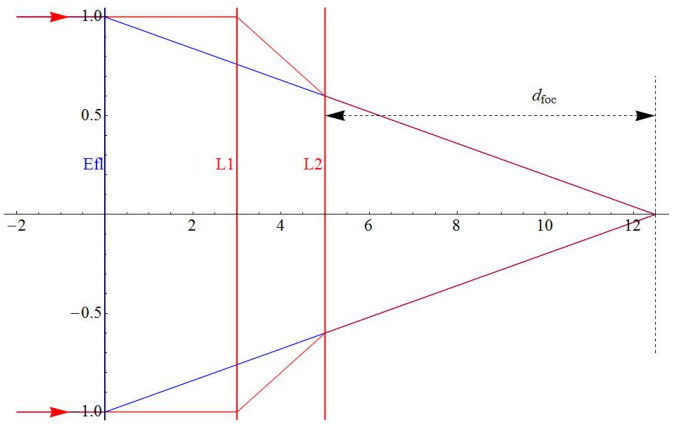

FIGURE 4.3: Efl

4.4 Brewster's angle

Light which strikes the interface of two (non-magnetic) media with the refraction indices n_1 and n_2 splits up in a reflected and a transmitted part. This splitting depend on the polarization of the incomming light. The electric field of the s-polarized part of the light is perpendicular to the plane spanned by the normal of the interface $-\vec{n}$ and the incoming ray. The electric field of the p-polarized part of the light is parallel to this plane.

One can calculate the *Intensity* of the reflected I_r and transmitted I_t part for each of this polarisations by the *Fresnel-Equations*[26]:

$$
\begin{aligned}
R_s(\alpha) &= \frac{I_r s}{I_0} = \left(\frac{n_1\ \cos(\alpha) - n_2\ \cos(\beta)}{n_1\ \cos(\alpha) + n_2\ \cos(\beta)}\right)^2 \\
R_p(\alpha) &= \frac{I_r p}{I_0} = \left(\frac{n_2\ \cos(\alpha) - n_1\ \cos(\beta)}{n_2\ \cos(\alpha) + n_1\ \cos(\beta)}\right)^2 \\
T_s(\alpha) &= \frac{\cos(\beta)}{\cos(\alpha)}\ \frac{I_t s}{I_0} = \frac{n_2\ \cos(\beta)}{n_1\ \cos(\alpha)}\ \left(\frac{2\ n_1\ \cos(\alpha)}{n_1\ \cos(\alpha) + n_2\ \cos(\beta)}\right)^2 \\
T_p(\alpha) &= \frac{\cos(\beta)}{\cos(\alpha)}\ \frac{I_t p}{I_0} = \frac{n_2\ \cos(\beta)}{n_1\ \cos(\alpha)}\ \left(\frac{2\ n_1\ \cos(\alpha)}{n_2\ \cos(\alpha) + n_1\ \cos(\beta)}\right)^2 .
\end{aligned}
\tag{4.19}
$$

Where the incident light has the intensity I_0 and makes an angle α to the normal of the interface. The angle of the transmitted light makes an angle β to $\vec{n}$ which is given by the *Snell's law*. As a consequence of conservation of energy, the *Reflectance* ($R_{s/p}$) and the *Transmittance* ($T_{s/p}$) of each polarisation sums up to one ($R_s + T_s = 1$, $R_p + T_p = 1$).

By inserting

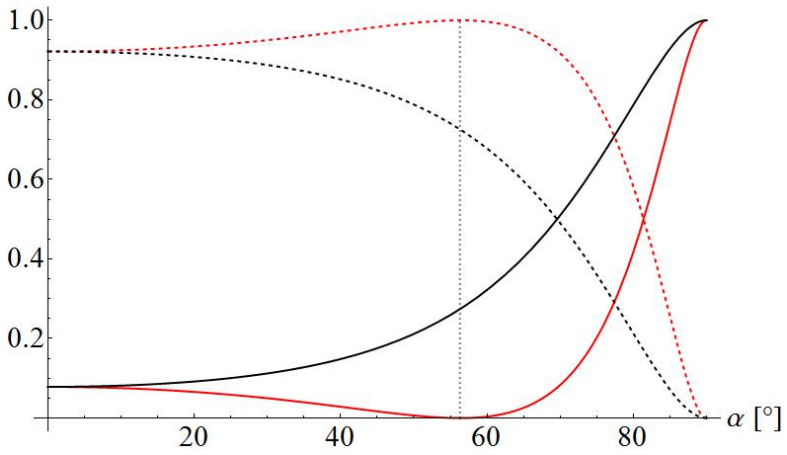

FIGURE 4.4: This Figure shows the transmittance (dashed line) and reflectance (solid line) of a glass window ($n_2 = 1{,}5$) exposed to air ($n_1 = 1$), as a function of the angle of incidence α. The vertical dotted line indicates the *Brewster's Angle*.

$$\alpha = \alpha_B = \arctan\left(\frac{n_2}{n_1}\right) \tag{4.20}$$

in Equation 4.19 one gets a reflectance of the p-polarized part of zero $R_p(\alpha_B) = 0$. The angle (α_B) is called the *Brewster's Angle*. The small amount of the light which gets reflected is therefore totaly s-polarized (see. Figure 4.4). The transmitted beam is still a mixture of s- and p-polarized light. *Polarizing Beam-Splitter* (PBS) use this effect at up to 100 layers with alternating indices of refraction. In this way all of the s-polarized part of the incident light gets reflected and the remaining part is totaly p-polarized. This system only works theoretically that perfect. Therefor we will use the *Extinction Ratio* to measure the performance of a PBS.

Within this thesis we want to define the extinction ratio of a PBS by:

$$\begin{aligned} Ext_p &= \frac{I_{tp}}{I_{rp}} = \frac{T_p}{R_p} = \frac{T_p}{1 - T_p} \\ Ext_s &= \frac{I_{rs}}{I_{ts}} = \frac{R_s}{T_s} = \frac{1 - T_s}{T_s}. \end{aligned} \tag{4.21}$$

Furthermore this ratio equals the *Signal to Noise Ratio* (SNR).

Chapter 5

Experimental Setup

A telescope will be used to collect the photons sent by Alice. Therefore, the first Section within this Chapter will present briefly the optical path through such telescopes.

Afterwards, a characterizing measurements of the optical elements, which where used for the receiver, will be presented.

The last two sections are introductions to the problems of polarization matching and clock synchronization.

5.1 Optical path

The calculations in this section give approximate results which are useful for planning a receiver. A more accurate study of the optical setup can be done by a software like *Zemax*.

The receiver will be attached to different telescopes. Doing so we have to take care of atmospheric turbulence. This turbulence causes *Angle of Arrival* fluctuations $\alpha = \frac{\beta}{2}$ in the range of 0,5μrad to 45μrad (see Section 4.2). The optical path of the light trough the telescope can be simplified to the one shown in Figure 4.1. Therefore, we can use Equation 4.13, with $V = \frac{f_{coll}}{f_{tel}}$, to calculate the fluctuations of the angle $\alpha_{coll} = \alpha_{l2}$, which is enclosed by the collimated beam and the z-axis:

$$\alpha_{l2} = -\frac{\alpha}{V} = -\frac{\alpha\, f_{tel}}{f_{coll}}. \tag{5.1}$$

If we use a Newton-Telescope with a focal length of the primary mirror (PM) of f_{PM} and a plane secondary mirror (SM), the focal length of the telescope f_{tel} equals f_{PM}.

The collimation lens with the focal length f_{coll} has to be placed at the right distance from the PM $x_{coll} = f_{PM} + f_{coll}$.

If the secondary mirror is not plane, like in a Cassegrain-Telescope, one can calculate f_{tel} with Equation 4.17:

$$f_{tel} = \frac{f_{PM}\ f_{SM}}{f_{PM} + f_{SM} - x_{PtS}}, \tag{5.2}$$

where f_{SM} is the focal length of the secondary mirror and x_{PtS} is the distance between those mirrors. The distance between PM and the collimation lens should be in this case (see Equation 4.18):

$$x_{coll} = \frac{f_{SM}\ (f_{SM} - x_{PtS})}{f_{PM} + f_{SM} - x_{PtS}} + x_{PtS} + f_{coll}. \tag{5.3}$$

The diameter of the collimated beam at the pupil plane is given by $d_{pup} = V\ d_{PM}$, where d_{PM} denotes the diameter of the primary mirror. Since the angular amplification of the atmospheric turbulence is proportional to $\frac{1}{V}$ there is a minimum cross section d_{spot}, which can be created with a lens placed at the distance x_{pl} from the last pupil plane (see Equation 4.14).

$$d_{spot}(d_{pup}) = 2\ \tan(\alpha_{coll})\ x_{pl} + d_{pup} = 2\ \tan\left(\frac{\alpha\ d_{PM}}{d_{pup}}\right)\ x_{pl} + d_{pup} \tag{5.4}$$

This minimum can be calculated by inserting:

$$d_{pup_{min}} \simeq \sqrt{2\ \alpha\ x_{pl}\ d_{PM}} \tag{5.5}$$

into Equation 5.4. With a large telescope with $d_{PM} \simeq 1m$, a distance $x_{pl} \simeq 1m$ and under bad weather conditions $\alpha \simeq 45\mu rad$ we get a optimum diameter of the collimated beam of $d_{pup_{min}} \simeq 1cm$. This corresponds to an amplification factor of $V \simeq \frac{1}{100}$.

To choose the right lens in front of the detector, we can calculate the angle of an incoming plane wave, which hits the Detector lens (L3) at its edge by rearranging

$$d_3 = 2\ \tan\left(\frac{\alpha_{edge}}{V}\right)\ x_{pl} + d_{pup} \simeq 2\ \frac{\alpha_{edge}}{V}\ x_{pl} + d_{pup} \tag{5.6}$$

to

$$\alpha_{edge} = \frac{d_3 - d_{pup}}{2\ x_{pl}}\ V. \tag{5.7}$$

Now we can determinate the focal length of this lens (f_3) in a way that this beam also hits the detector on its edge. Therefore we use Equation 4.15 and rearrange $FoV = 2\ \alpha_{edge}$ to:

$$f_3 = \frac{x_{pl}\ d_{det}}{d_3 - d_{pup}}. \tag{5.8}$$

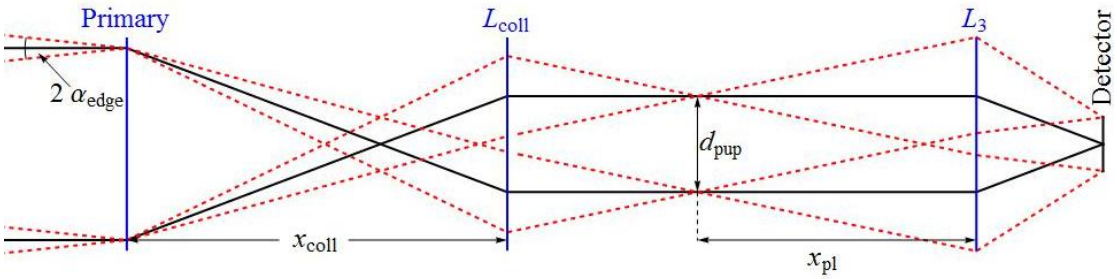

FIGURE 5.1: pupillenabbildungTelscope

Inserting the values from above, a detector-size of $d_{det} = 0{,}5mm$ and, a diameter of L_3 of $d_3 = 25mm$ results to a focal length of $f_3 \simeq 3cm$.

At some telescopes you have little space for a receiver. Therefore, I have built the $8mm$-Bob with small optical components (aperture of $\sim 1cm$). Currently this system is attached to the Newton-Telescope at the IQOQI-Vienna, which has a primary mirror with diameter $d_{PM} = 40cm$ an focal length $f_{PM} = 120cm$. The light gets collimated with a lens of focal length $f_{coll} = 3{,}5cm$. Two further lenses ($f_{a1} = 7{,}5cm$ and $f_{a2} = 2{,}5cm$) reduce the beam by a factor of $V = \frac{f_{PM}\ f_{a1}}{f_{coll}\ f_{a2}} \simeq \frac{1}{103}$ to $d_{pup} = \frac{d_{PM}}{103} \simeq 0{,}4cm$. If we use Equation 5.4 with $x_{pl} = 40cm$ and $\alpha = 45\mu rad$ we get a result $d_{pup_{min}} \simeq 0{,}38cm$ which is very close to d_{pup}. This means that we are already close to smallest spot size at the lens in front of the detectors, which calculates according to Equation 5.4 to $d_{spot} = 0{,}76cm$. Since the aperture of the detector lens is $d_3 = 8mm$, the light cone is thin enough for fitting through.

The lenses in this system have got a focal length of $f_3 = 8mm$. This results in a Field of view of the detectors of $FoV = 600\mu rad$. This large FoV is not used since the small aperture fades out everything with a larger angular distance of $45\mu rad$ this equals a Field of View of $90\mu rad$. Even this small receiver is nearly to heavy for this mount. But the stability of the telescope was enough for the first measurements at a stationary link.

This $8mm$-Bob attached to a the OGS in Cephalonia ($d_{PM} = 1{,}4m$) would result, according to an equivalent calculation, to a FoV of $\sim 5\mu rad$. A bigger FoV can only be

achieved by optics with a bigger aperture. Therefore a second receiver with the aperture of $1''$ was built.

5.2 Optical Elements

The properties of the optical elements, used for the $8mm$ receiver, have been measured before assembly. The light source for these measurements was a laser diode which emit a wave length of $\lambda = 808nm$. This wavelength was shifted with an external grating stabilisation to $810nm$, which is equivalent to the beam splitter source. The light was coupled to a single mode fibre to get a Gaussian shaped beam. The intensity was regulated by *Neutral Density Filters* and the fibre-coupling efficiency. The Polarization of the light was controlled by a linear polarizer and a half-wave-plate and its *Extinction ratio* was $Ext > 21000$. The results of this measurement will be presented in the following subsections.

5.2.1 50:50 Beam Splitter

A *50:50 Beam Splitter* consist of two right triangle prisms, glued together with their surface at the hypotenuse. Between those prisms is a thin metallic layer combined with different other layers. Since the light is able to enter several nm into the metal (evanescent wave), one can chose the splitting ratio of the BS by varying the thickness of the layer. The reflectivity of the used metal varies with the polarization of the light and therefore introducing some unwanted effects.

Figure 5.2 shows a measurement of the percentage based intensity in the reflected I_R (red points) and transmitted I_T (blue pints) arm during a 90° rotation of the half-wave plate of the source. The black lines are fit functions of the form

$$I_{R/T}(\gamma) = A_{R/T}\ \cos^2\left(B_{R/T}\ \frac{\pi}{180} + \gamma\right) + D_{R/T} \tag{5.9}$$

	A	**B**	**D**
Transmitted	0,0432	0,2627	0,4752
Reflected	−0,0432	0,2627	0,5248

with the fitting parameters $A_{R/T}$, $B_{R/T}$, $D_{R/T}$ and, the pitch angle γ. This polarization dependence of the beam splitter leads to a change of the state of polarization during transmission/reflection which is described by the coefficients Z_{pR}, Z_{sR}, Z_{pT} and, Z_{sT}:

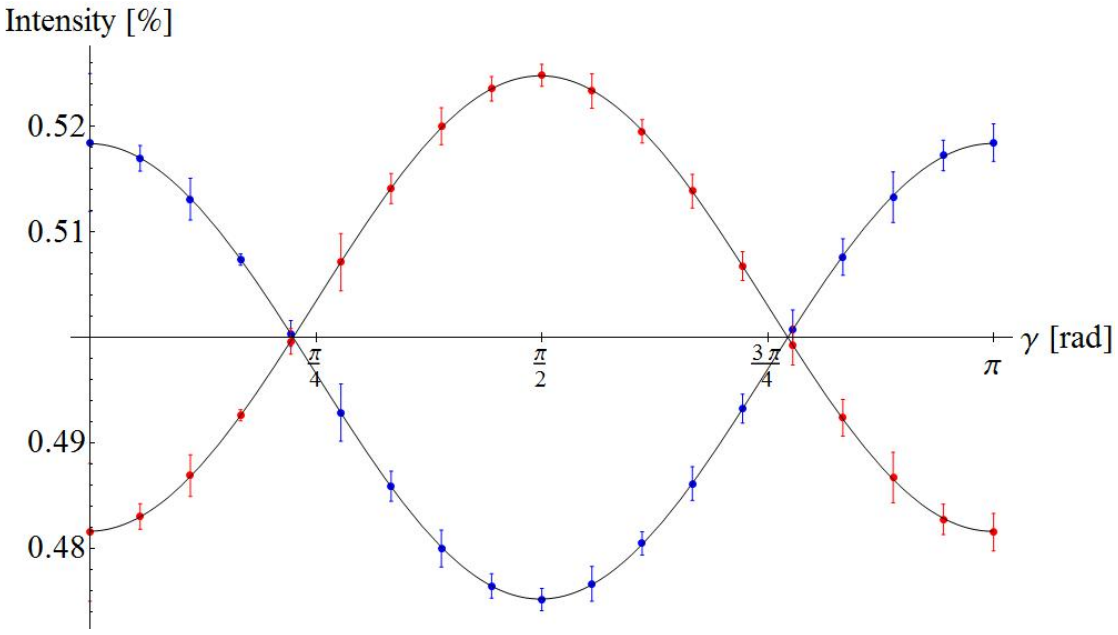

FIGURE 5.2: Measurement of the polarization dependence of the Beam Splitter used. The red and blue points correspond to the reflected and transmitted arm, respectively. The black lines are fitted functions of the form 5.9. γ ist the polarization-angle ($\gamma = 0$ or $\pi \Rightarrow$ H-polarization, $\gamma = \frac{\pi}{2} \Rightarrow$ V-polarization). The wavelength of the laser was $810nm$ and its average power was $80\mu W$.

$$\begin{gathered} \sin(\gamma)|H\rangle + \cos(\gamma)e^{i\varphi}|V\rangle \\ \Downarrow \\ \sin(\gamma)\ Z_{pR/T}\ |H\rangle + \cos(\gamma)\ Z_{sR/T}\ |V\rangle. \end{gathered} \tag{5.10}$$

For one layer these four numbers can be calculated with the *Fresnel-Equations* and depend on the index of refraction of the layer. In the case of a metallic layer these coefficients will be complex and induce a phase-shift between the Horizontal and the Vertical polarized components [26] which can be easily corrected with wave-plates. In the calculation below, we assume the complex part of $Z_{p/sR/T}$ as negligibly small. The probability of Reflection/Transmission of H/V-polarized light $P_{H/VR/T}$ can be calculated by:

$$\begin{aligned} P_{HR/T} &= |Z_{pR/T}|^2 = I_{R/T}(0) \simeq A_{R/T} + D_{R/T} \\ P_{VR/T} &= |Z_{sR/T}|^2 = I_{R/T}(\frac{\pi}{2}) \simeq D_{R/T}. \end{aligned} \tag{5.11}$$

We can further calculate the change of the pitch angle $\Delta\gamma_{R/T}$ for an initial state of $|\pm 45°\rangle$:

$$\Delta\gamma_{R/T} = \gamma_{R/T} - \gamma = \arctan\left(\pm\sqrt{\frac{A_{R/T} + D_{R/T}}{D_{R/T}}}\right) \mp \frac{\pi}{4}. \tag{5.12}$$

Inserting in the fitting parameters from above results to $\Delta\gamma_R = \mp 1{,}23°$ and $\Delta\gamma_T = \pm 1{,}24°$ where the upper sign and lower sign are valid for an initial state of $|+45°\rangle$ and $|-45°\rangle$, respectively.

This means the pitch angle difference between the incoming states $|+45°\rangle$ and $|-45°\rangle$ is shifted after the BS and calculates for the reflected and the transmitted beam to 87,54° and $92,48°$, respectively. This shift leads to polarization errors and can not be corrected in this system. Nevertheless, the receiver works properly since this deviation is quite small (see Chapter 6).

5.2.2 Polarising Beam Splitter

A *Polarising Beam Splitter* (PBS) consists of two prisms which are glued together at their surface at the hypotenuse. Between these prisms a large number (up to 100) of layers with alternating index of refraction act like a dielectric mirror. The refraction indices of the prisms and the layers are designed in a way that the light hits the layers of the mirror at the *Brewster's angle*. At this angle the reflectivity of the interfaces equals zero for the horizontal polarized light (see. Section 4.4)[26]. This splitting takes place at every intersection between the layers. Because of the structure of the mirror all those parts interfere with each other and result in a reflected and a transmitted beam, well polarized at V and H, respectively.

The performance of a PBS strongly depends on the angle of arriving of the incoming light. We expect a fluctuation of this angle caused by atmospheric turbulence ($\beta = 85...17\mu rad$ Section 4.2) amplified by the telescope by a factor of roughly 100 which results to 0,5° (FWHM of the Angular spread). The following experimental results present the performance of PBS in this angular range.

Figure 5.3 shows the *Extinction Ratio* (Equation 4.21) of two PBS for horizontal polarized light (Ext_p). The angle ϕ between the incoming beam and the normal of the cube $\vec{n}$ varied from $-4°$ to $4°$ during the measurement. One can see clearly that these PBS work best by tilting them at $\phi_{max} = 1{,}8°$ and 1,25° out of back-reflection ($\vec{n} \parallel$ incoming light).The blue shaded area indicates the expected FWHM angular spread of the received beam of $\pm 0{,}25°$. The extinction in this area varies less than the peak difference of the two PBS which are caused by the production tolerances.

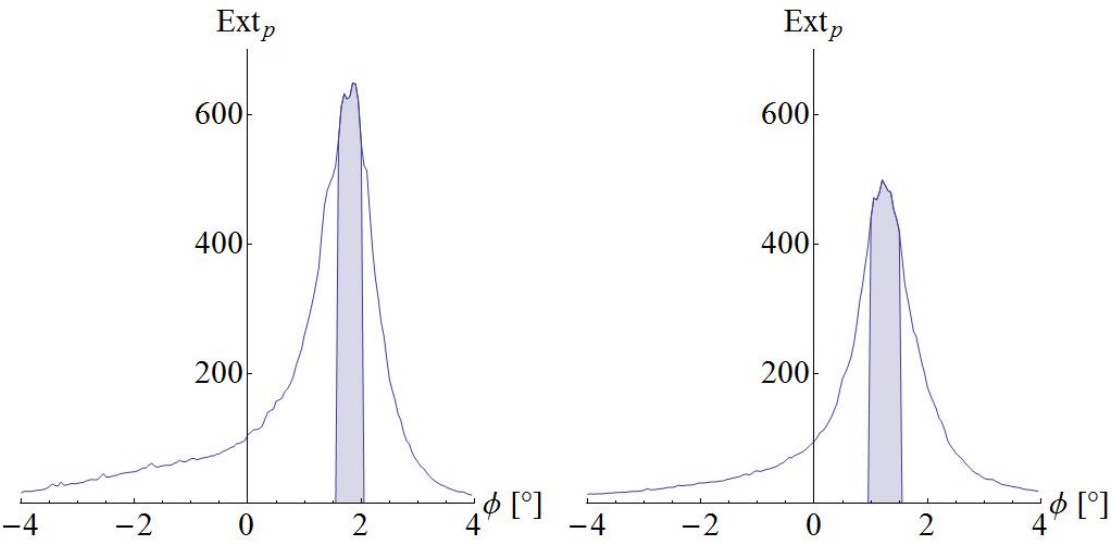

FIGURE 5.3: Extinction Ratio measurement of two PBS for horizontal polarized light (Ext_p) as a function of the cube tilt ϕ. The blue shaded area indicates the expected FWHM angular spread of ±0,25°.

So these PBS can be used for free-space experiments without a significant drop of the extinction ratio. But the rotation of the beam splitters would lead to a decreased clear aperture in the *Cage-Cube-System* since the reflected beam would make an angle of 2 ϕ_{max} to the central axis of the system. This leads to a spot at the detectors-lens which is z_{PL} $\tan(2\phi_{max})$ of axis. So it is necessary to keep the distance between the PBS and the lens z_{PL} as short as possible.

The same measurement for two PBS from an other manufacturer (Bernhard Halle) are presented in Figure 5.4. These beam-splitters work for a much broader angular range and the Extinction at back-reflection is nearly as high as the peak of the curve. Figure 5.5 shows the same measurement of those two PBS but with vertical polarized light (Ext_s).

The reason for the nearly flat distribution of the Extinction can be found in Equation 4.20. The reflectance for s-polarized light ($R_s(\alpha)$) is not quite high but after more than 100 interfaces (between the prisms of the PBS) almost all of the s-polarized light is reflected. This process is nearly independent of the angle of incidence. In the case of p-polarized light, a high Extinction can only be achieved if the light hits every interface of the layers at the Brewster's angle. This leads to the peak like function in Figure 5.4 and 5.3.

Based on the presented measurements the second pair of PBS has been placed into the receiver.

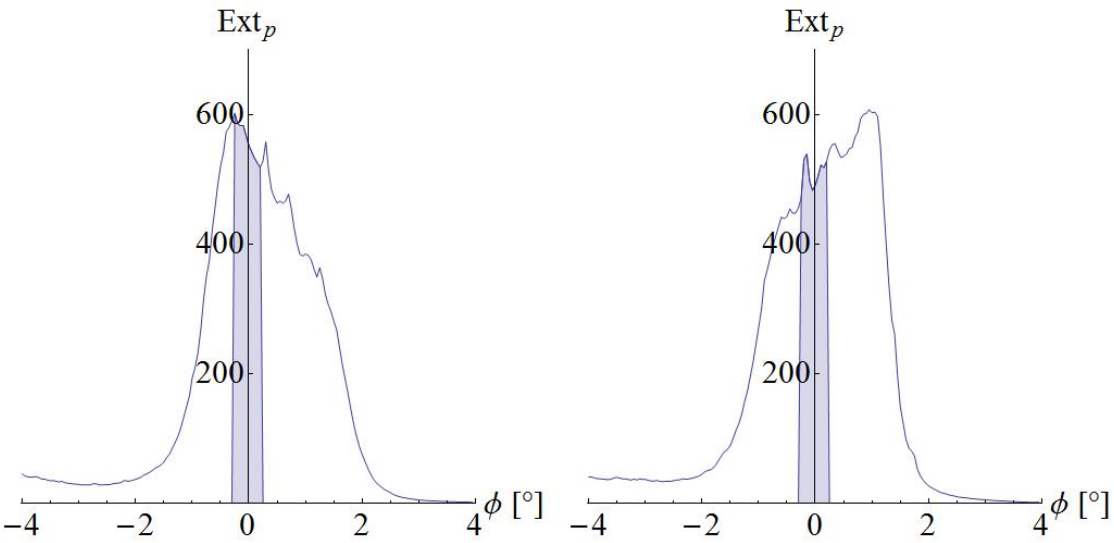

FIGURE 5.4: Extinction Ratio measurement of two PBS for horizontal polarized light (Ext_p) as a function of the cube tilt ϕ. The blue shaded area indicates the expected FWHM angular spread of ±0,25°.

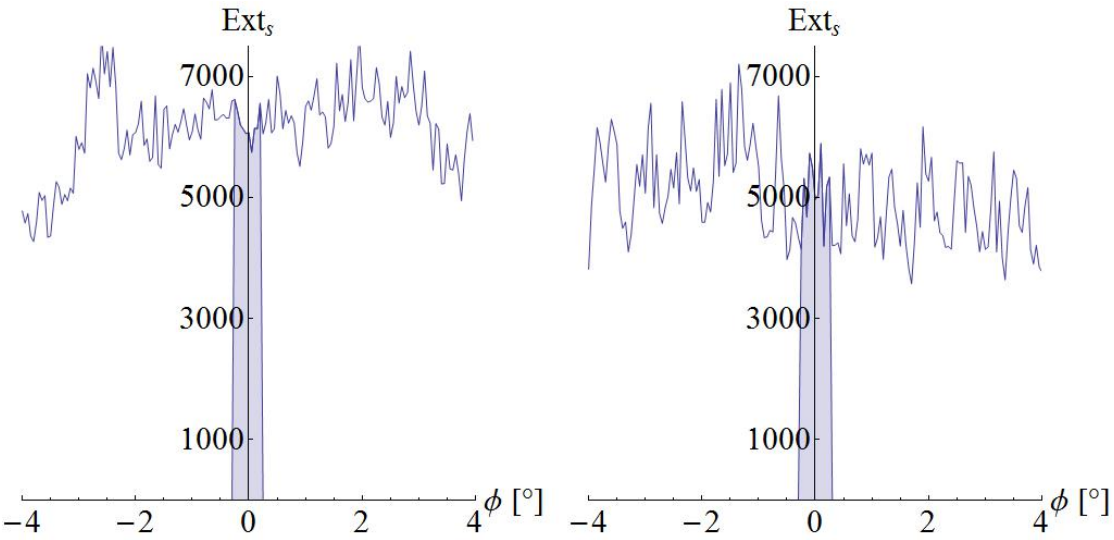

FIGURE 5.5: Extinction Ratio measurement of two PBS for vertical polarized light (Ext_s) as a function of the cube tilt ϕ. The blue shaded area indicates the expected FWHM angular spread of ±0,25°.

5.2.3 Filters

A *Dielectric Filter* combined with a *Colored Glass Filter* are used as an entrance-window for the receiver. Those filters block out the light which is not in the spectral range expected from the sender.

Dielectric Filter consist of several layers of dielectric material. The thickness and the refraction index of the layers are designed so that a broad spectral range of light gets reflected but a small spectral range is transmitted. The transmittance of the used filter

is shown as red line in Figure 5.6. The central wavelength of the transmitted spectral range is $809nm$ with a FWHM of $3nm$. One can see that the dielectric filter starts to be transparent for light with a shorter wavelength then $600nm$. Therefore we have placed an additional colored glass filter which blocks out this wavelength range (blue line in Figure 5.6).The filter also starts to be transparent for light with a wavelength larger than $1300nm$ but this is no problem since the efficiency of the detector is close to zero at this wavelength.

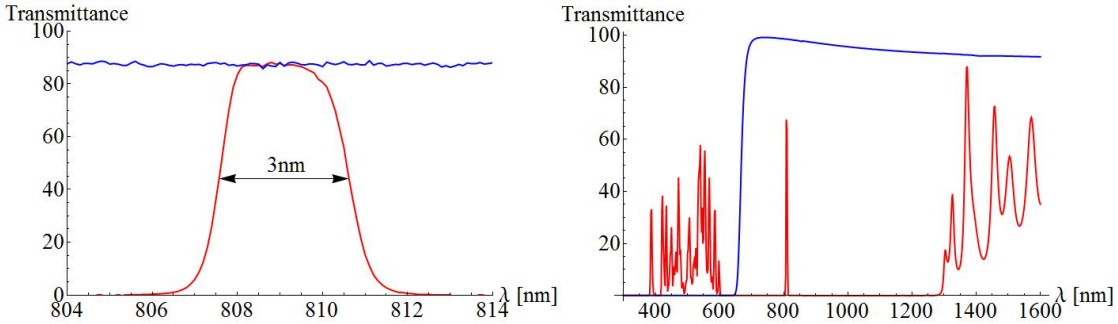

FIGURE 5.6: Transmittance of the colored glass filter (blue) and the interference filter (red) as a function of the wavelength λ. The left graph shows a detailed measurement of region of interest around $809nm$. The right graph shows a measurement of the full spectrum of the spectrometer.

The dielectric filters are designed for use with an angle of arrival α of $0°$. Since we expect angular fluctuations of the beam on the order of $\frac{FWHM}{2} = 0.25°$, we further want to investigate the behaviour of the filter during tilt. The layers of the filter act like a thin Fabry-Pèrot etalon [27] with an effective index of refraction n_{eff}. This value can be found in the data-sheet of every filter. The phase difference between the directly transmitted beam and a beam which gets m-times reflected before it is transmitted is given by $\Delta\varphi$ [26]:

$$\Delta\varphi = \frac{2\,\pi}{\lambda}\, m\, \Delta s \tag{5.13}$$

with an optical path difference of

$$\Delta s = 2\, d\, \sqrt{n_{eff}^2 - \sin^2(\alpha)} \tag{5.14}$$

Constructive interference of all of the m-times reflected beams and therefore a maximum transmission is given if $\Delta\varphi = l\ 2\pi$ which is equal to $\Delta s = l\ \lambda$. In those equations d denotes the thickness of the layers and l and m are integers. This leads to a maximum transition at a tilting angle $\alpha = 0$ for the wavelength

$$\lambda_{max}(0) = \lambda_d = 2\ d\ n_{eff} \tag{5.15}$$

where the index d in λ_d should indicate that this is the wavelength for which the filter was designed for. If we know λ_d and n_{eff}, we can calculate the shift of the central wavelength of the Filter during tilt by:

$$\lambda_{max}(\alpha) = \lambda_d \sqrt{1 - \frac{\sin^2(\alpha)}{n_{eff}^2}}. \tag{5.16}$$

This calculation is a rough approximation for a dielectric filter but works very well for small α. For a larger angle of incidence one has to consider the polarization dependence of the reflectance and transmittance of the individual layers. A more precise calculation which considers those effects can be found in [28].

If we calculate the change of the central wavelength ($\lambda_d = 809nm$) with the expected angle of arrival of $\alpha = 0.25°$ and an effective index of $n_{eff} = 2.08$ we get $\lambda_{max}(0.25°) = 808{,}998nm$. This change of $\delta\lambda = -0{,}002nm$ is negligibly small compared to the FWHM of $3nm$.

The colored glass filter is made of glass to which various absorptive materials have been added. Therefore the performance of this filter is almost independent of the angle of incidence.

The glowing of the detectors after detecting a photon (see Section 5.2.4) can lead to a "crosstalk" between different detectors in the module. This is because the emitted light is distributed over a broad spectral range and apart of it is therefore reflected, by the dielectric filter, back towards the detectors. This additional noise destructed the first measurements. The solution for this problem is to mount the filter tilted at an angle $> 5°$. In this way the reflected light can't hit any other detector. The calculated cental wavelength-shift for 5° results to a negligible small number of $\Delta\lambda = -0{,}77nm$.

For the $8mm$ aperture receiver a fast solution was needed. So we squeezed a small ball of paper between the mount and the filter. All results within this thesis from the $8mm$ aperture receiver have been measured with the *paper-ball-filter*. Since this method is not quite precise a more beautiful solution has been chosen for the $1''$-receiver. We used a 3D-Printer to produce wedge-shaped tubes which replaces the paper-ball. The measurement results for this filter with and without wedged-tube are presented in Figure 5.7.

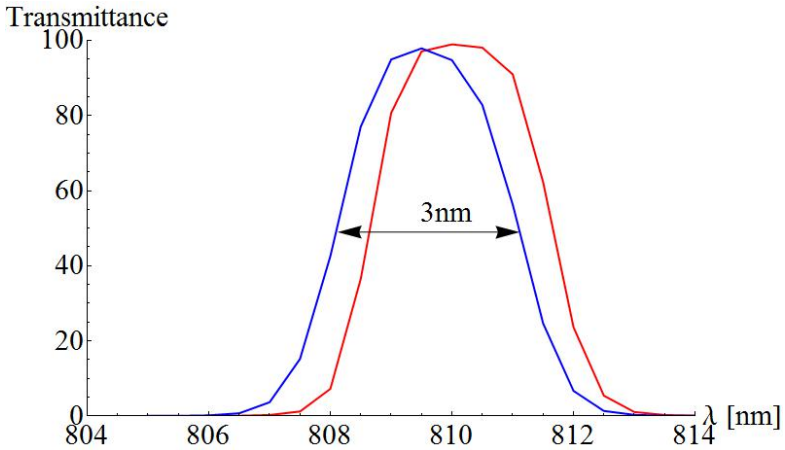

FIGURE 5.7: Measurement of the filter for the $25mm$ aperture receiver with (blue) and without (red) wedged-tube mount

The red line in Figure 5.7 shows the transmittance of the filter without tilt. The central wavelength is $\lambda_{max}(0°) = 810{,}4nm$ and the measured FWHM is $3nm$. The blue line indicates the transmitted spectrum with a tilt of $\alpha = 5°$. The shifted central wavelength has been measured to be $\lambda_{max}(5°) = 809{,}73nm$. This results in a $\Delta\lambda$ of $-0{,}67nm$ and fits quite fine to the calculations. One can see that the shifted wavelength-transmission-window still covers $810nm$ at which the beam-splitter source (Section 3.7) works. This wavelength is now closer to the border of the window but the transmission is still at 94,8%.

Since the decoy source of the satellite emits light at a wavelength of $850nm$ a different filter was measured, too. Based on the calculation from above a filter with $\alpha_d = 552nm$ has been bought and a tilt tube for 8° was printed. The measurement for this filter is presented in Figure 5.8, showing the shift of the transmission peak to exactly $850nm$.

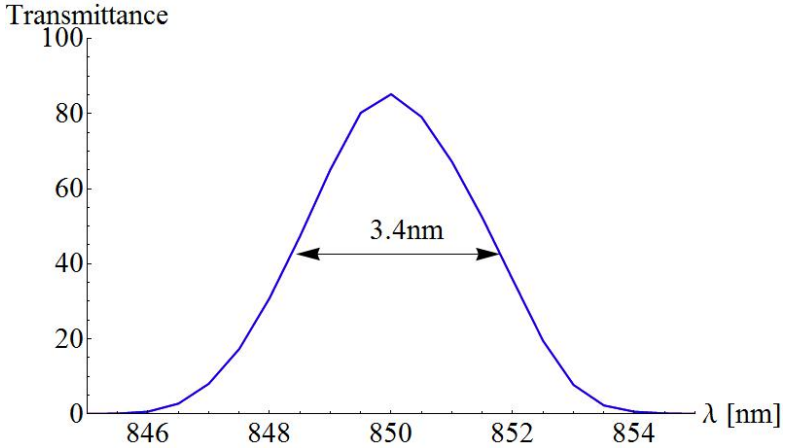

FIGURE 5.8: Measurement of the $852nm$ filter for the $25mm$ aperture receiver with 8° tilt-tube-mount.

5.2.4 Detectors

The detectors used consist of *Silicon Avalanche Photodiodes* (Si-APD) which are implemented in an electrical circuit which operates the diode in the Geiger mode. In this mode, the bias voltage V_{bias} of the diode is applied in reverse direction and exceeds the breakdown voltage V_{br} by an amount of $V_E = V_{bias} - V_{br}$. Free electrons get accelerated by the space charge in the diode and create further free electrons by impact ionization. If V_{bias} is in the region described above, one single electron is able to trigger a self-sustaining avalanche of charge carriers (Geiger shower) which is a measurable current [29]. This process continues as long as the bias voltage is above the breakdown voltage. The so called *quenching circuit* lowers V_{bias} to stop the avalanche and restores the voltage afterwards. In the easiest case this circuit consists of a resistor in series with the diode (*passive quenching*). The time span between the leading edge of the avalanche until the bias voltage is restored is called the *Dead Time* t_D of the detector. This time can be reduced by using an *active quenched* system which measures the diode current and lowers the bias voltage actively. Free electrons can also occur due to thermal ionization which lead to an avalanche without the presence of a photon at the diode (*Dark Counts*). Those dark counts grow exponentially with the temperature [30]. Therefore a thermoelectric cooler within the housing of the diode is used to decrease the temperature of the diode. Another property of the diode is the *Detection efficiency* η which is a product of the *quantum efficiency* and the *breakdown probability*. Where the quantum efficiency is the number of generated primary electron-hole pairs per incident photon and the breakdown probability is the chance that a free electron causes an avalanche.

For the $8mm$-Receiver a detector was developed by the Austrian Institute of Technology (AIT). The housing of these passive quenched detectors is small enough to fit to the used cube system. Two potentiometers offer the possibility to adjust the bias voltage and the temperature of the diode. To achieve a big FoV of the detector a diode with large active area (SAP500 Laser Components. Inc., $500\mu m$ diameter) was built in. According to the measurements for this diode presented in [30], the temperature was set to $-22.5°C$ and V_{bias} was set such that 200 dark counts resulted. A rough measurement of the detection efficiency was performed with an attenuated laser ($\lambda = 810nm$) and a reference detector which resulted in 55%. More information about this detector can be found in Appendix A.

Laser Components offer single photon counting modules for the near infrared spectrum with an active area diameter of the diodes of $100\mu m$. Those detectors are used in the $1''$-Receiver. The biggest Field of View feasible with those diodes is $50\mu rad \simeq 10arcsec$ (Equation 4.15, $f_3 = 2cm$ and, $V = \frac{1}{100}$). An equivalent counting module with the same $500\mu m$ diodes as used for the AIT-detectors will be available soon. Those counting

modules are the best choice for the 1″-Receiver, since the biggest feasible FoV with those diodes is five times larger.

We expect a dark count rate and efficiency of the Laser Components detectors to be in the same range as measured for the AIT-detectors. The main difference between the two systems will be a shorter dead time of the LC-detectors, since those will be active quenched.

As previously mentioned in Section 5.2.3 a *crosstalk* between the detectors occurred during the first measurements. This effect increased the noise within the receiver dramatically. The reason for this crosstalk was a glowing of the detectors which is known in the literature as *Hot-carrier luminescence* in reverse biased p-n junctions [31] and which is well studied for arrays of photon-counting avalanche-diodes [32]. The noise level was back to normal (intrinsic dark counts) when the reflective filter at the entrance window of the receiver was tilted with more than 5°.

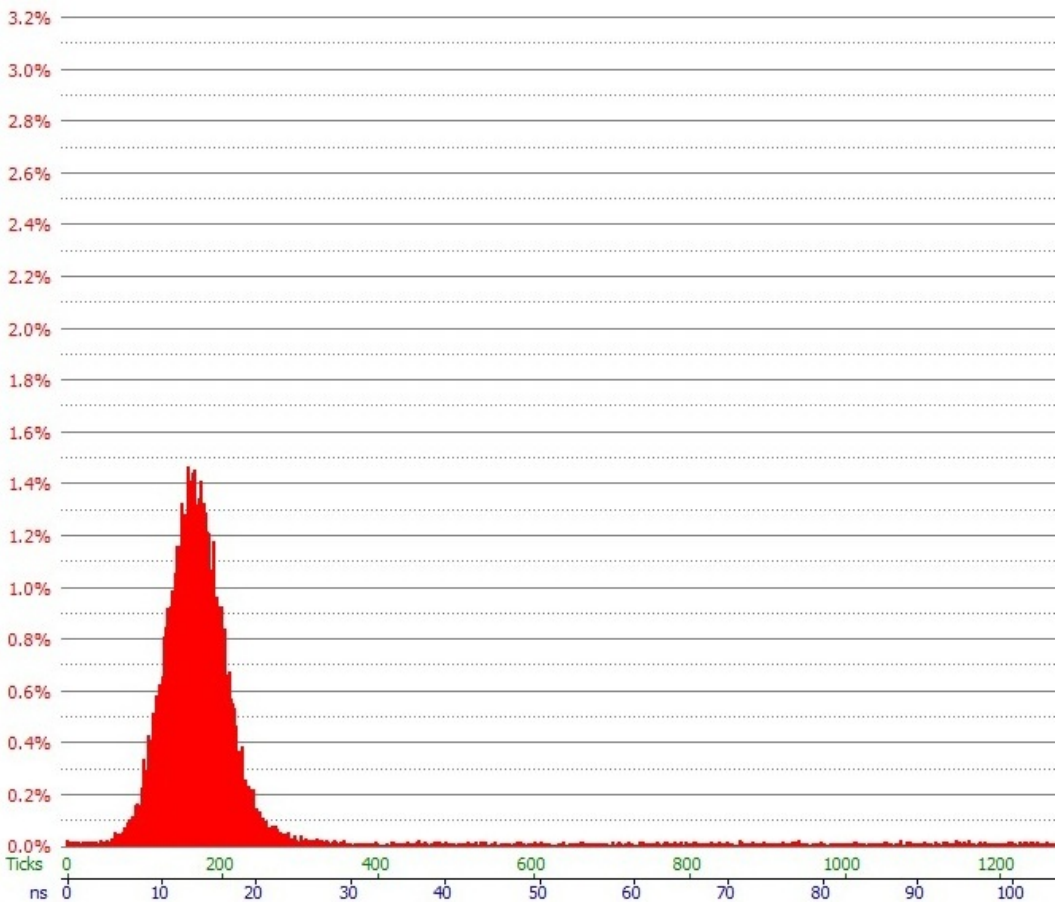

FIGURE 5.9: Delay Histogram of a start-stop measurement between two detectors. During this measurement the filter-tilt was zero

One can further think of using this effect for a side channel in quantum cryptography systems. The successful photon measurements at the detector result $11ns$ later (Figure

5.9) to the emission of a bunch of photons in a certain spectral range. The optical path from the primary mirror of the telescope to the detectors can be reversed and the PBS-cubes on this path act like polarizers. The filter at the entrance is transparent for photons within the spectral-transmission-window (See Figure 5.8). An eavesdropper could place a dichroic mirror between Alice and Bob which transmits the photons from Alice and reflects those photons from the detector-glowing into a structurally identical receiver module. Therefore, Eve would be able to detect which detector of Bob lights up.

It is planned to investigate the gain of information for Eve in such scenarios. Therefore, the total number of emitted photons per avalanche and their spectral range should be measured.

5.3 Polarization matching

When attempting to analyze the polarization of light from a source at the satellite, one have to take into account the time dependent difference between the reference system at the sender and the receiver. Also the pointing mirrors will influence the polarization during a passover. This polarization mismatch will be compensated with a motorized QHQ-combination. There is no chance to verify the correct position of the wave-plates during the measurement. Therefore, we have two options. We can either use the tracking laser as reference polarization and calculate the right QHQ positions from this signal, or we calculate those positions without a reference.

For the latter option we want to follow the model presented in [33]. Let's consider a satellite with its orbital plane at a certain angle to the equatorial plane of earth with a source on board which emits light tangential to its orbit (see Figure 5.10).

In this scenario at least one movable fine pointing mirror is needed to deflect the light to the ground station. The change of polarization caused thereby is described by a *Jones matrix* $\mathbf{M}(\alpha, \beta)$:

$$\mathbf{M}(\alpha, \beta) = \begin{pmatrix} r_p(\alpha) & 0 \\ 0 & r_s(\alpha) \end{pmatrix} \times \mathbf{R}(-\beta), \tag{5.17}$$

where α is the angle of incidence of the light at the mirror, $r_p(\alpha) = \sqrt{R_p(\alpha)}$ and, $r_s(\alpha) = \sqrt{R_s(\alpha)}$ are given by Equation 4.20. The matrix $\mathbf{R}(\beta)$ (Equation 3.10) decomposes the $|H\rangle$ and $|V\rangle$ components of the senders light into S and P components in which the mirror is described (see Section 4.4). The complex index of refraction of a metallic

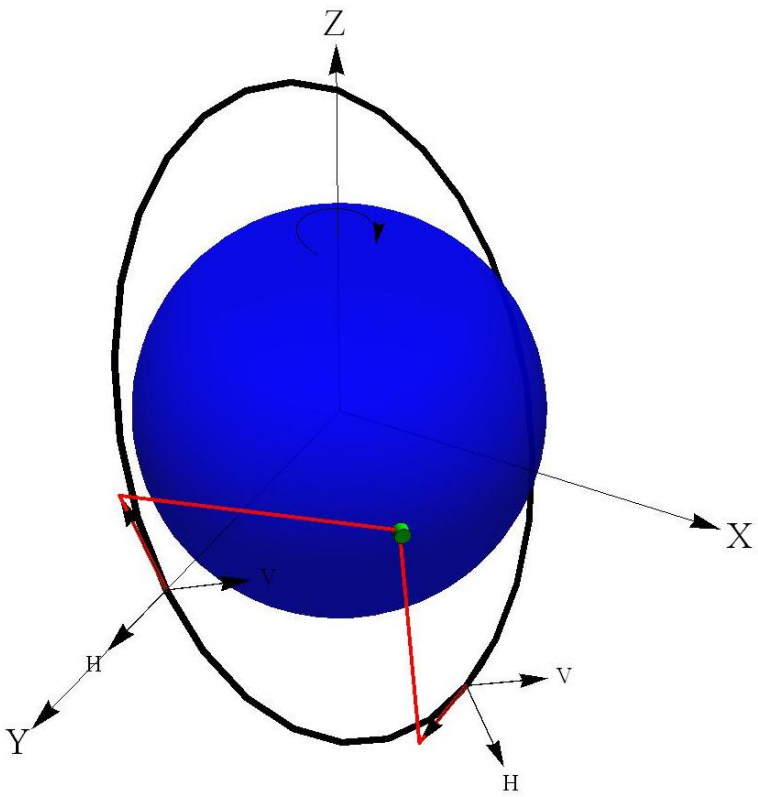

FIGURE 5.10: Satellite orbit (black ring) around the earth (blue sphere). The Satellite emits light (red line) tangential to it's orbit which gets reflected at a movable mirror. This mirror directs the light towards an OGS (green). The figure illustrates the satellite at two different positions on it's orbit.

mirror leads to a complex matrix **M** and will therefore introduce a phase shift between the S- and P-Polarized components.

A second fine pointing mirror at the ground station can be used to deflect the light from the moving telescope to the receiver. The polarization transformation matrix $\mathbf{M_2}$ for such systems can be calculated by:

$$\begin{aligned}&\mathbf{M_2}(\alpha, \beta, \alpha_2, \beta_2, \beta_3) = \\ &\mathbf{R}(\beta_3) \times \begin{pmatrix} r_p(\alpha_2) & 0 \\ 0 & r_s(\alpha_2) \end{pmatrix} \times \mathbf{R}(\beta_2) \times \begin{pmatrix} r_p(\alpha) & 0 \\ 0 & r_s(\alpha) \end{pmatrix} \times \mathbf{R}(-\beta),\end{aligned} \tag{5.18}$$

where α_2 is the angle of incidence of the light at the secund mirror, $\mathbf{R}(\beta_2)$ takes the mismatch of the S and P components of the first and the secund mirror into account and $\mathbf{R}(\beta_3)$ considers the difference between the $|H\rangle$ and $|V\rangle$ components of the receiver and the S and P components of the second mirror. The five time-dependent angles in

$\mathbf{M_2}(\alpha, \beta, \alpha_2, \beta_2, \beta_3)$ can be calculated with the coordinates of the ground station and the satellite orbit date [33].

The motorized QHQ-combination at the receiver can be used to compensate the change of polarization during a pass over of the satellite. In the following we take a closer look at a reflection at only one mirror $\mathbf{M_1}(\alpha, \beta, \beta_2)$ compensated with a QHQ-combination. The change of the polarization after transition through such a system is described by the matrix $\mathbf{T}$:

$$\begin{aligned}\mathbf{T}(\alpha, \beta, \beta_2) &= \mathbf{QHQ}(q_2(\beta), h(\alpha, \beta, \beta_2), q(\beta_2)) \times \mathbf{M_1}(\alpha, \beta, \beta_2) \\ &= \mathbf{QWP}(q_2(\beta)) \times \mathbf{HWP}(h(\alpha, \beta, \beta_2)) \times \mathbf{QWP}(q(\beta_2)) \times \\ &\quad \mathbf{R}(\beta_2) \times \begin{pmatrix} r_p(\alpha) & 0 \\ 0 & r_s(\alpha) \end{pmatrix} \times \mathbf{R}(-\beta),\end{aligned} \tag{5.19}$$

With the angular positions of the wave-plates

$$\begin{aligned} q_2(\beta) &= \beta + \frac{\pi}{4}, \\ h(\alpha, \beta, \beta_2) &= \frac{\arg_p(\alpha) - arg_s(\alpha)}{4} + \frac{\beta + \beta_2}{2} - \frac{\pi}{4}, \\ q(\beta_2) &= \beta_2 + \frac{\pi}{4} \quad with \\ arg_p(\alpha) &= \arctan\left(\frac{Im[r_p(\alpha)]}{Re[r_p(\alpha)]}\right) \quad and, \\ arg_s(\alpha) &= \arctan\left(\frac{Im[r_s(\alpha)]}{Re[r_s(\alpha)]}\right) \end{aligned} \tag{5.20}$$

the transformation matrix $\mathbf{T}$ results to:

$$\begin{aligned}\mathbf{T}(\alpha, \beta, \beta_2) = e^{i*(arg_p + arg_s)} \times \frac{|r_p| + |r_s|}{2} \times \\ \left[\begin{pmatrix} 1 & 0 \\ 0 & 1 \end{pmatrix} + \frac{|r_p| - |r_s|}{|r_p| + |r_s|} \begin{pmatrix} \cos(2\,\beta) & \sin(2\,\beta) \\ \sin(2\,\beta) & -\cos(2\,\beta) \end{pmatrix}\right].\end{aligned} \tag{5.21}$$

Equation 5.21 shows a matrix dependent on $r_p(\alpha), r_s(\alpha)$ and, β which is equal to the identity if $|r_p(\alpha)| = 1$ and $|r_s(\alpha)| = 1$. We get the state of polarization of linear polarized light after transition through this system by multiplying the Jones-vector of the initial state with $\mathbf{T}$:

$$
\begin{aligned}
&\mathbf{T} \times \begin{pmatrix} \cos(\gamma) \\ \sin(\gamma) \end{pmatrix} = \\
&\quad e^{i*(arg_p+arg_s)} \, \frac{|r_p|+|r_s|}{2} \begin{pmatrix} \cos(\gamma) + \frac{|r_p|-|r_s|}{|r_p|+|r_s|} \cos(2\,\beta-\gamma) \\ \sin(\gamma) + \frac{|r_p|-|r_s|}{|r_p|+|r_s|} \sin(2\,\beta-\gamma) \end{pmatrix} \\
&\quad = A\, e^{i*(arg_p+arg_s)} \begin{pmatrix} \cos(\gamma_2) \\ \sin(\gamma_2) \end{pmatrix} \quad \textit{with} \\
&A = \frac{1}{\sqrt{2}} \sqrt{|r_p|^2 + |r_s|^2 + (|r_p|^2 - |r_s|^2)\, \cos(2\,\beta - 2\,\gamma)} \quad \textit{and} \\
&\gamma_2 = \arctan\left(\frac{\sin(\gamma) + \frac{|r_p|-|r_s|}{|r_p|+|r_s|} \sin(2\,\beta-\gamma)}{\cos(\gamma) + \frac{|r_p|-|r_s|}{|r_p|+|r_s|} \cos(2\,\beta-\gamma)} \right)
\end{aligned}
\tag{5.22}
$$

where γ denotes the pitch angle which is enclosed by the polarization axis of the linear polarized light and the horizontal axis. The exponential term in Equation 5.22 is a global phase-shift which has no effect on the state of polarization. The further terms in 5.22 describe the losses at the mirror which can not be corrected with wave-plates and result in a shift of the pitch angle.

We can see that the angles chosen in 5.20 are the best choice if we put some numbers in Equation 5.22 and calculate the resulting pitch angle γ_2.

Initial Pol.	γ	β	γ_2
$\|H\rangle$	0	0	0
$\|V\rangle$	$\frac{\pi}{2}$	0	$\frac{\pi}{2}$
$\|+45°\rangle$	$\frac{\pi}{4}$	0	$\arctan\left(\frac{\|r_s\|}{\|r_p\|}\right) \simeq \frac{\pi}{4} + \frac{\|r_s\|-\|r_p\|}{2\,\|r_p\|}$
$\|+45°\rangle$	$-\frac{\pi}{4}$	0	$-\arctan\left(\frac{\|r_s\|}{\|r_p\|}\right) \simeq -\frac{\pi}{4} - \frac{\|r_s\|-\|r_p\|}{2\,\|r_p\|}$
$\|H\rangle$	0	$\frac{\pi}{4}$	$\arctan\left(\frac{\|r_s\|-\|r_p\|}{\|r_s\|+\|r_p\|}\right) \simeq \frac{\|r_s\|-\|r_p\|}{\|r_s\|+\|r_p\|}$
$\|V\rangle$	$\frac{\pi}{2}$	$\frac{\pi}{4}$	$\arctan\left(\frac{\|r_s\|+\|r_p\|}{\|r_s\|-\|r_p\|}\right) \simeq \frac{\pi}{2} - \frac{\|r_s\|-\|r_p\|}{\|r_s\|+\|r_p\|}$
$\|+45°\rangle$	$\frac{\pi}{4}$	$\frac{\pi}{4}$	$\frac{\pi}{4}$
$\|+45°\rangle$	$-\frac{\pi}{4}$	$\frac{\pi}{4}$	$-\frac{\pi}{4}$

with $\beta = 0$ or $\beta = \frac{\pi}{4}$ meaning the incoming and reflected light at the mirror are in the horizontal or vertical plane of the source, respectively. From the chart above one can see clearly a pitch-angle shift which leads for $\beta = 0$ to an angular distance $\Delta\gamma_2$ between $|+45°\rangle$ and $|-45°\rangle$:

$$
\Delta\gamma_2 \simeq \frac{\pi}{2} + \frac{|r_s| - |r_p|}{|r_p|} \neq \frac{\pi}{2}. \tag{5.23}
$$

Therefore any further adjustments to correct the shift for $|+45°\rangle$ would lead to a greater shift for $|-45°\rangle$ and vice versa. This small polarization mismatch leads to an additional noise in the receiver. The *Signal to Noise Ratio* of such a one-mirror-system has been calculated for unprotected gold, silver and aluminium mirrors. The results of this calculation represents an upper limit for the achievable SNR which is shown in Figure 5.11.

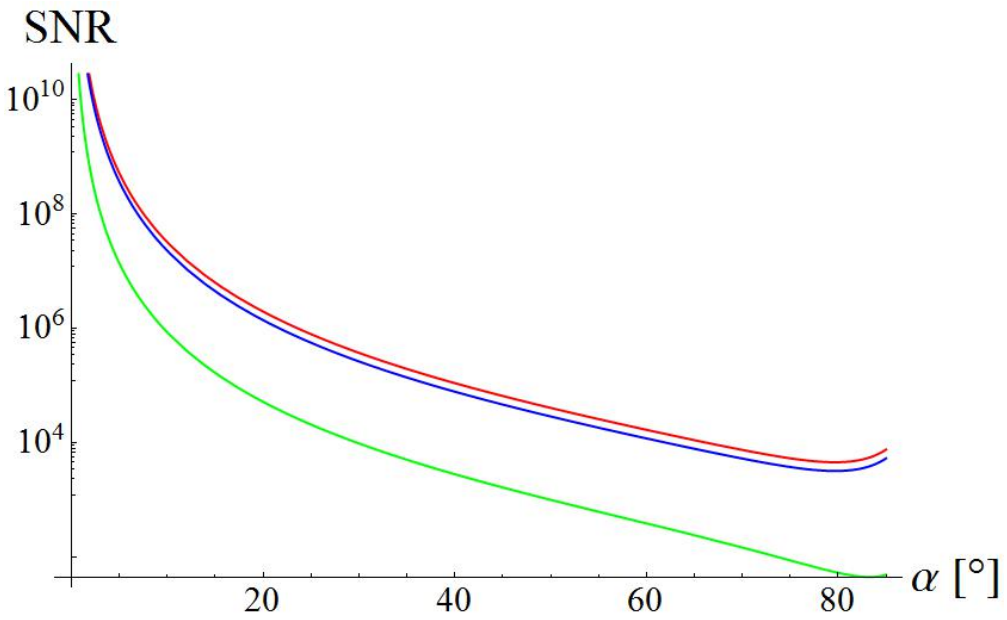

FIGURE 5.11: Calculated SNR in the $|\pm 45°\rangle$ basis, as a function of the angle of incidence at the mirror. The considered noise is caused by a polarisation mismatch described above. The red, blue and, green line represent the results for unprotected gold ($n_{Au} = 0.16408 - i5.3194$), silver($n_{Ag} = 0.19620 - i5.3347$) and, aluminium($n_{Al} = 2.5041 - i8.0052$) at $\lambda = 850nm$, respectively

A SNR higher than 10^4 corresponds to a visibility of $> 99{,}9\%$. Therefore, the errors introduced by a gold or silver mirror should be negligibly small. Aluminium mirrors can cause some trouble, when used with an angle of incidence larger than 60°. I want to note that the calculated SNR in Figure 5.11 corresponds to uncoated metallic mirrors. Optical coatings reduce the described effect, but their refraction index depends on the coating used. To realise such a compensation scheme, a measurement of the refraction index of all movable mirrors is required.

5.4 Tracking and Clock Synchronisation

In order to keep the signal from the satellite in the FoV of the detectors, an accurate tracking system will be used. Therefore, the satellite overlaps its quantum signal ($\lambda = 850nm$) with a green tracking laser ($\lambda_G = 532nm$). A dichroic mirror which is reflective

for infra red and transparent for green light can be used to separate those two signals. A part of the green light which is pulsed with a repetition rate of $10kHz$ will be used to trigger a single photon detector which generates the synchronisation pulse for the clock at the ground station (See Figure 5.12). The rest of the light gets focused to a tracking camera. The picture of this camera can be used to adjust the position of the telescope. An additional tracking ($\lambda_R = 671nm$) laser will be sent from the ground station to the satellite. Doing so, the satellite is able to correct it's sending direction (bidirectional tracking).

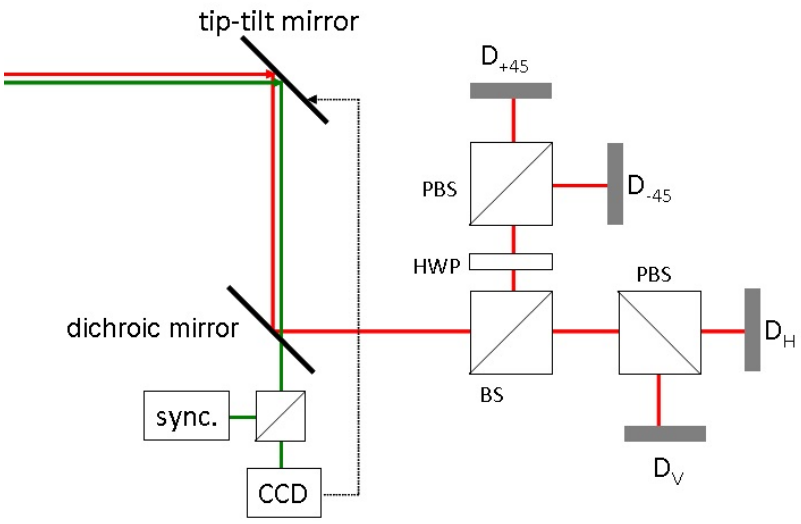

FIGURE 5.12: Tracking scheme, Picture made by Thomas Scheidl

The pointing error of state of the art telescopes, with such systems, is less then $1arcsc$. For telescopes with bigger pointing errors one can improve the system with an additional tip-tilt-mirror within the optical path as depicted in Figure 5.12. If this mirror is placed in the pupil plane of the telescope, a pointing correction without introducing a beam offset can be achieved.

Chapter 6

Results

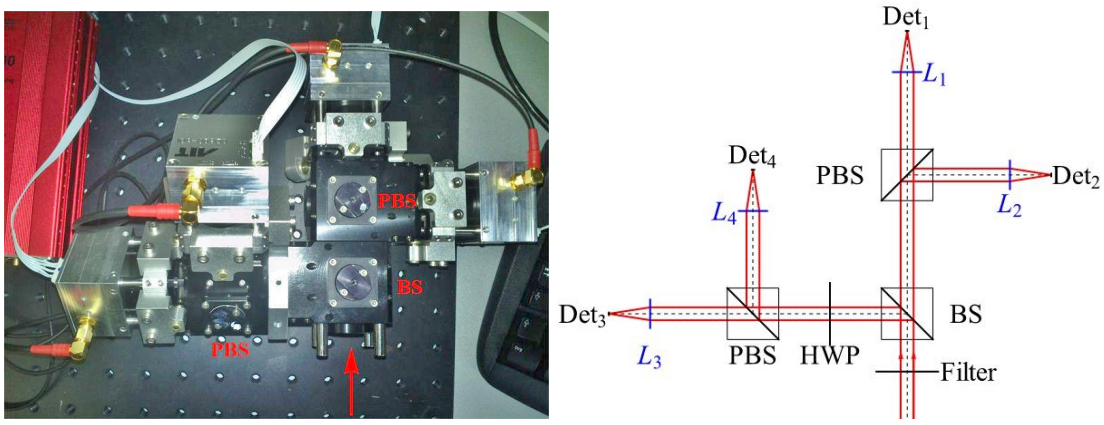

FIGURE 6.1: *Left*: Picture of the $8mm$-receiver. *Right*: Schematic drawing of the receiver. The photons enter the module through an interference filter (red arrow) and get either transmitted or reflected at the *Beam Splitter* (BS). Passing one of the two *Polarizing Beam Splitter* (PBS) and one of the *Lenses* (L_i), each photon ends up in one of the four *Detectors* (Det_i)

The optical elements of both receivers are mounted in a *Cage/Cube-System*. The whole Bob module is therefore easily mounted and is not dependent on the presence of a *Breadboard*. The cubes are also light tight which makes it unnecessary to put the set-up into a Black Box. Further advantages of the Cage/Cube-System is the small size ($18 \times 28{,}5cm$) and the resistance against vibration. With all these properties the receiver should fit into a broad range of telescopes.

The $1''$-receiver is still under construction but it's smaller brother is already attached to the telescope on the roof of the IQOQI-Vienna. Before the receiver was placed there a measurements in the laboratory was performed. The source for this experiment was an attenuated laser using the set-up described in Section 5.2. The data of this measurement reveal the performance of the receiver under perfect (laboratory) conditions. Afterwards

the Bob module was attached to the telescope. The measurement presented in the last section shows the visibility of polarization after a $10km$ free space link.

6.1 Measurements with attenuated laser

For the measurement presented in this section an attenuated continuous wave laser ($\lambda = 810nm$) was coupled to the receiver. The polarization of the beam was modulated with a HWP resulting in a pitch angle γ between by the polarization axis and the horizontal axis.

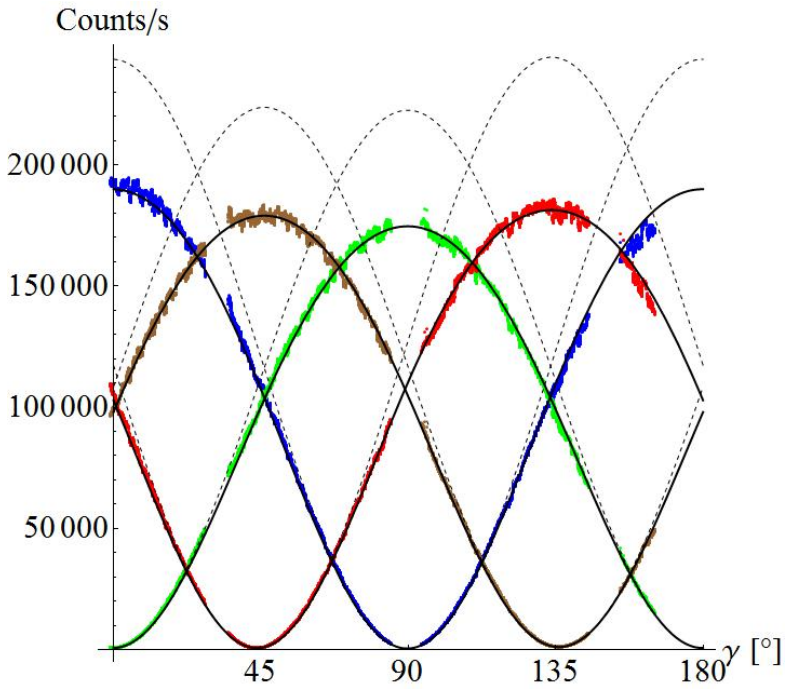

FIGURE 6.2: Count rate of the four detectors of the receiver during a rotation of the pitch angle of the incoming polarization γ with a mean count rate of $97000 Couns/s$. The blue, green brown and red points represent measurements of the H-, V-,+45°- and −45°-detectors, respectively. The black solid lines are fit-curves of the form 6.1. The dashed lines show the expected count rates for linear detectors [$f_{fit2}(\gamma, G = 0)$ see Equation 6.2].

Figure 6.2 shows the four detector count rates at different HWP positions with a mean count rate of $97000 Couns/s$ at each detector. The expected fit-function for such a measurement would be:

$$f_{fit1}(\gamma) = A \ \cos^2(\gamma + B) \tag{6.1}$$

Where A and B denote the total count rate and a mismatch of γ, respectively. But the dead time of the passive quenched detectors leads to a count rate which is not linear

with the rate of photons arriving at the detector. Using passive quenched detectors one can observe this effect for count rates above $100000 Counts/s$.

Therefore, I used a fit-function of the form:

$$f_{fit2}(\gamma) = -G\, f_{fit1}^2(\gamma) + f_{fit1}(\gamma) + D, \tag{6.2}$$

where f_{fit1} is the number of photons per second arriving at the detector and f_fit2 is the count rate of the detector. This count rate has got an offset D which represents the sum of counts resulting from background light and dark-counts, while G considers the non-linearity of the detector.

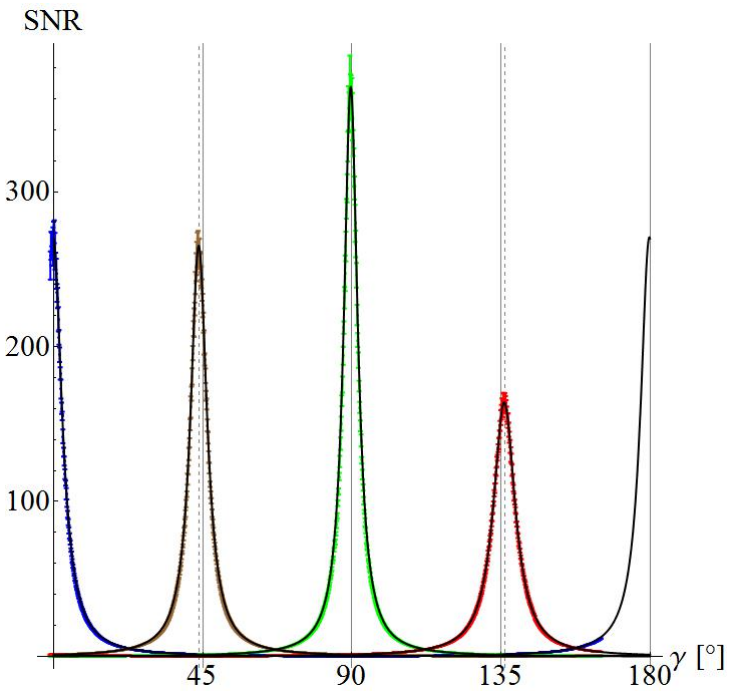

FIGURE 6.3: Signal to noise ratio of the four detectors during a rotation of the pitch angle of the incoming polarization γ. The solid vertical lines at $\gamma = 0°,\ 45°,\ 90°,\ 135°$ represent the incoming polarization states H-, V-,+45°- and $-45°$, respectively. The dashed lines indicates the maxima of the curves. The different heights of the maxima is caused by a different non-linearity and dark count rates of the detectors. Also the various extinction ratio of the optical elements within the module influence the height of the maxima (See Section 5.2.1 and 5.2.2)

Figure 6.3 shows the obtained (SNR)

$$SNR_H = \frac{Counts_H/s}{Counts_V/s}, \quad SNR_V = \frac{Counts_V/s}{Counts_H/s}, \tag{6.3}$$

$$SNR_{+45} = \frac{Counts_{+45}/s}{Counts_{-45}/s} \ \ and, \quad SNR_{-45} = \frac{Counts_{-45}/s}{Counts_{+45}/s} \tag{6.4}$$

for this measurement. In this figure one can see clearly a shift of the maxima of the SNR in the $\pm 45°$-basis. This shift can be calculated to $\Delta\gamma_{+45\ max} = B_{-45} + 45° = -1{,}0°$ and $\Delta\gamma_{-45\ max} = B_{+45} - 45° = 1{,}2°$. The measurement fits perfectly to the shift $\Delta\gamma_R = \mp 1{,}23°$, calculated in Section 5.2.1, which is caused by the polarization dependence of the 50:50-beam-splitter.

From these results one can calculate a visibility as presented in the table below. For the corrected values the *Dark Count rate* of the detectors ($DC_{DetH} = 205 \pm 14$, $DC_{DetV} = 205 \pm 14$, $DC_{Det+45} = 185 \pm 14$, $DC_{Det-45} = 115 \pm 11$) was subtracted.

	$\|H\rangle$	$\|V\rangle$	$\|+45°\rangle$	$\|-45°\rangle$
Visibility uncorrected	$99{,}26 \pm 0{,}03$	$99{,}45 \pm 0{,}02$	$99{,}12 \pm 0{,}03$	$98{,}71 \pm 0{,}04$
Visibility corrected	$99{,}47 \pm 0{,}03$	$99{,}64 \pm 0{,}02$	$99{,}25 \pm 0{,}03$	$98{,}91 \pm 0{,}05$

The non-linearity of the detectors, at these count rates, is the limiting factor for the visibility. Therefore, the measurement was repeated with a mean count rate of $8640 Counts/s$. The results are presented in Figure 6.4 and the Visibilities are given in the table below.

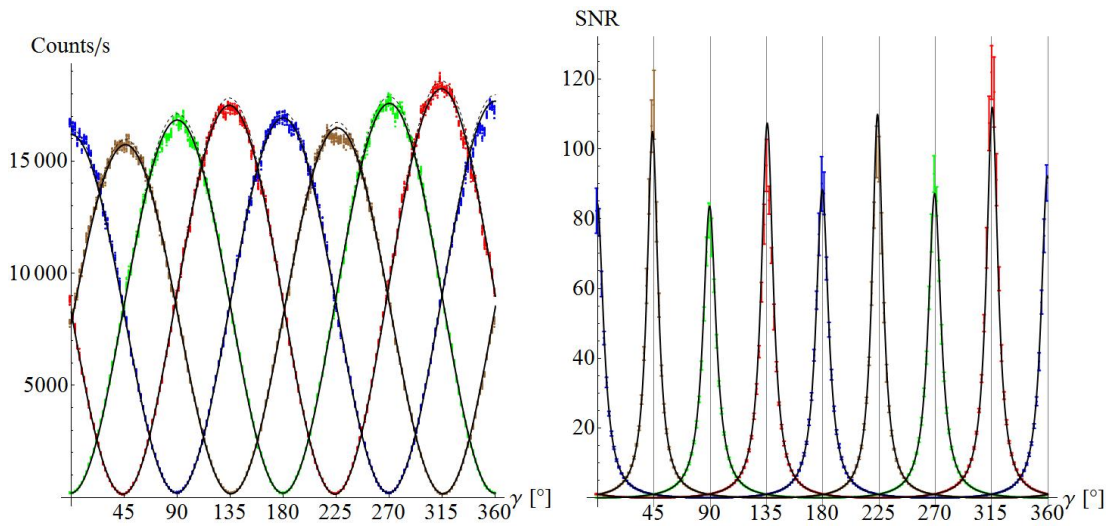

FIGURE 6.4: **Left:** Count rate of the four detectors of the receiver during a rotation of the pitch angle of the incoming polarization γ with a mean count rate of $8640 Counts/s$. The blue, green brown and red points represent measurements of the H-, V-,+45°- and $-45°$-detectors, respectively. The black solid lines are fit-curves of the form 6.1. The dashed lines show the expected count rates for linear detectors ($G = 0$). **Right:** Signal to noise ratio of the four detectors during a rotation of the pitch angle of the incoming polarization γ. The solid vertical lines at $\gamma = 0°,\ 45°,\ 90°,\ 135°$ represent the incoming polarization states H-, V-,+45°- and $-45°$, respectively. The different heights of the maxima is caused by a different dark count rate of the detectors and various extinction ratio of the optical elements within the module.

	$\|H\rangle$	$\|V\rangle$	$\|+45°\rangle$	$\|-45°\rangle$
Visibility uncorrected	$97{,}49 \pm 0{,}12$	$97{,}50 \pm 0{,}16$	$98{,}23 \pm 0{,}14$	$97{,}91 \pm 0{,}16$
Visibility corrected	$99{,}95 \pm 0{,}21$	$99{,}89 \pm 0{,}24$	$99{,}67 \pm 0{,}20$	$100{,}02 \pm 0{,}23$

The fluctuations of the subtracted dark count rate result in a corrected visibility of above 100%. This result shows that the limiting factor for the visibility is the dark count rate of the detectors. In QKD experiments, only dark counts which appear in a small time window ($\sim 1ns$), where photons are expected, affect the QBER (see Section 3.8 and 3.4). This happens with a probability, which is in the order of 10^{-7}, for the measured dark counts. We expect therefore a visibility, in laboratory based QKD experiments, similar to the corrected values in the table above. The lowest of those values is 99,8% which is very good compared to the boundary for QKD which is 70,7%.

6.2 Free Space Measurements

FIGURE 6.5: Distance between the telescope and the corner cube. Picture made with Google Earth v.7.1.2.2041

The Telescope in Vienna was utilized for the measurement presented in this chapter. An attenuated laser beam with a diameter of roughly $4cm$ and a wavelength of $808nm$ was directed from the rooftop of IQOQI-Vienna to a corner cube which was placed on the hills at the border of the city (See Figure 6.5 and 6.6). The light reflected from the corner cube was collected with a Newton-telescope with a diameter of the primary mirror of $40cm$. The attenuation over this 10km-link (5km distance) was about $-70dB$, mainly caused due to geometrical losses at the corner cube. The optical path through the telescope to the detectors is described in Section 5.1.

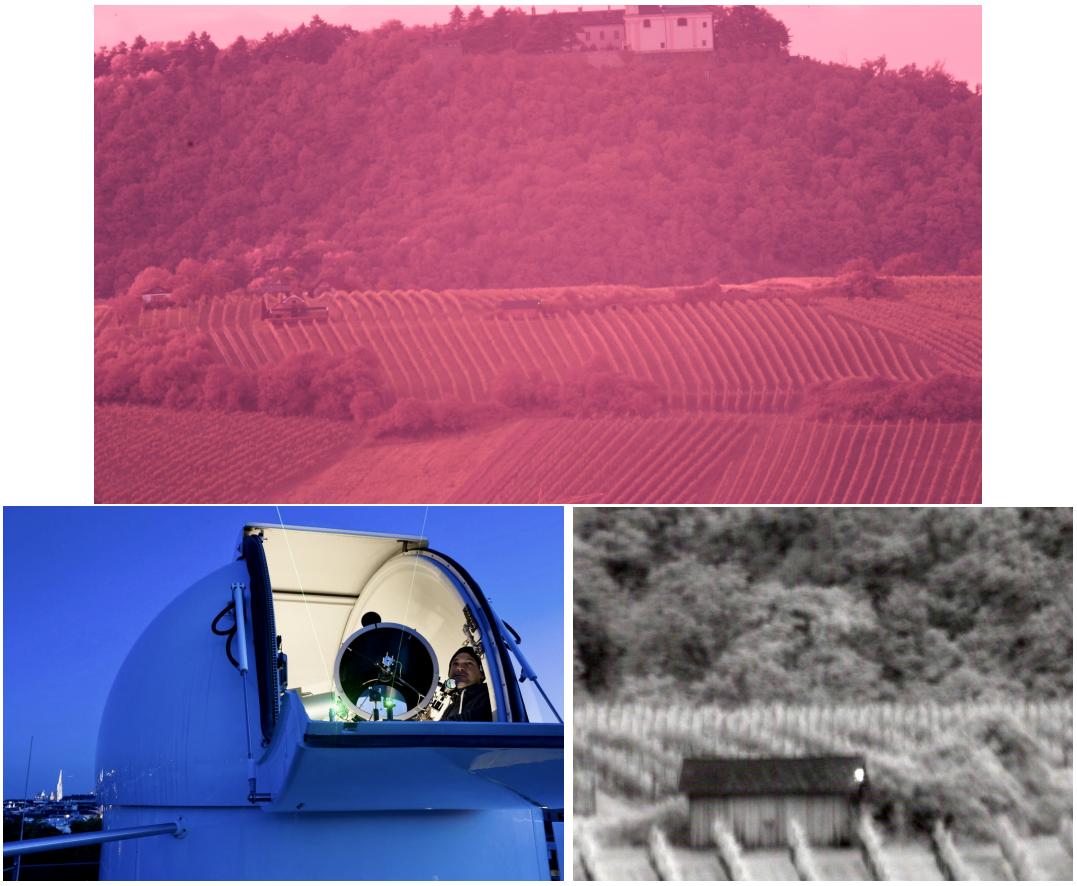

FIGURE 6.6: *Top:* Picture of the vineyards next to Vienna ,taken by the EOS camera at the guiding telescope. One can see the hut with the corner cube in the center. *Bottom right:* Picture of the hut, taken by the tracking camera of the Telescope. The bright spot is the $532nm$ beacon laser, reflected by the corner cube. *Bottom left:* Picture of the Hedy Lamarr Telescope, taken by Alois Lammerhuber.

Before the measurement one of the detectors was replaced by a camera. The observed FWHM diameter of the spot was $d_{FWHM} = 13\mu m$. This gives a seeing angle of $\beta = 15{,}5\mu rad$ (See Section 4.2).

During the measurement, the polarization was manipulated with a quarter-wave-plat while the count-rates of the four detectors were recorded (Figure 6.7,Left). The resulting Signal to Noise Ratio is shown in Figure (6.7,Right). From this data one arrives at the visibilities presented in the table below. The corrected values within this table where calculated by subtracting the background counts ($C_{DetH} = 1445 \pm 104$, $C_{DetV} = 1346 \pm 83$, $C_{Det+45} = 1033 \pm 75$, $C_{Det-45} = 859 \pm 68$) which correspond to a measurement with a blocked sender.

	$\|H\rangle$	$\|V\rangle$	$\|+45°\rangle$	$\|-45°\rangle$
Visibility uncorrected	$93{,}12 \pm 0{,}43$	$91{,}41 \pm 0{,}38$	$91{,}84 \pm 0{,}99$	$93{,}25 \pm 0{,}34$
Visibility corrected	$98{,}48 \pm 0{,}43$	$97{,}63 \pm 0{,}54$	$95{,}86 \pm 0{,}80$	$96{,}87 \pm 0{,}60$

The measurement night was a bit foggy, with the fog concentrated close to the ground. The light from the town reflected by the fog was the main source of noise. Further measurements of background counts, for which the telescope was directed at the almost clear sky, are presented in the table below. Generally, the background counts can be decreased by a more narrow filter, if necessary.

Altitude	C_{DetH}	C_{DetV}	C_{Det+45}	C_{Det-45}
45°	605 ± 48	522 ± 451	351 ± 36	321 ± 40
90°	581 ± 32	566 ± 50	399 ± 40	352 ± 50

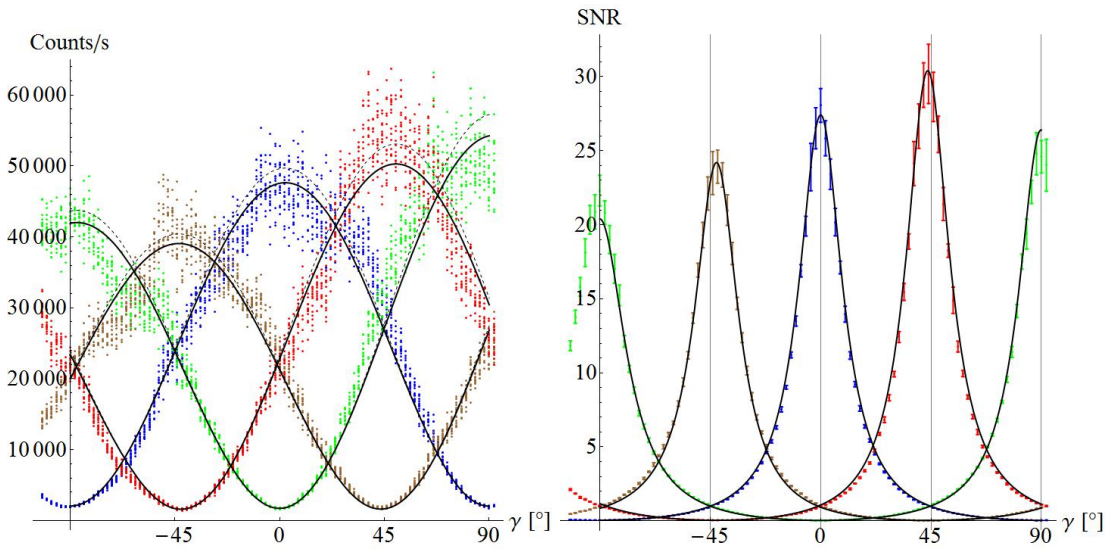

FIGURE 6.7: **Left:** Count rate of the four detectors of the receiver during a rotation of the pitch angle of the sent polarization γ with a mean count rate of $24200 Counts/s$. The blue, green brown and red points represent measurements of the H-, V-,+45°- and −45°-detectors, respectively. The black solid lines are fit-curves of the form 6.1. The dashed lines show the expected count rates for linear detectors ($G = 0$). **Right:** Signal to noise ratio of the four detectors during a rotation of the pitch angle of the sent polarization γ. The vertical lines at $\gamma = 0°,\ 45°,\ 90°,\ 135°$ represent the incoming polarization states H-, V-,+45°- and −45°, respectively. The different heights of the maxima is caused by a different dark count rate of the detectors and various extinction ratio of the optical elements within the module.

All measured visibilities are, even without dark count correction, above the boundaries for QKD. The difference between the visibilities measured in the laboratory and at the link, can be caused, e.g. by depolarisation of the corner cube, backscattered light from the atmosphere or depolarisation due to the optical path in the telescope. A measurement between a Alice, built with the sending telescope (see Section 3.7.1.3) and the beam-splitter source, and the ground station, could clarify the origin of the error, if necessary.

Chapter 7

Conclusion

Within this thesis I presented an approach for realization of the first quantum space-to-ground link with several ground station in Europe and a Chinese satellite. With a few calculations I gave an impression about the important properties for the successful realization of such experiments. I showed how to select the components for a receiver, fulfilling these properties. Furthermore, two receivers have been built and presented. A measurement with one of those receivers over a free space link of 10km was performed. The observed errors within this measurement are below the calculated boundaries for QKD and fundamental tests of nature. Therefore a successful satellite link with such a set-up is possible.

Furthermore, the effect of the detectors, which might be used as a side channel, was discussed. Measurements with respect to this effect can be done to investigate the quality of such attacks. The problem of polarization matching was presented. Further calculations and measurements can be done to check how accurate such a compensation scheme will work in a space-to-ground link.

The OGS-Vienna was used to perform the measurement of a 10km free space link. During which I noticed, that required equipment was too heavy for this telescope. The weight of the set-up will not be a problem for other ground stations, but in this particular case a different solution has to be found. A new mount for this ground station, which fulfills the required dynamic pointing accuracy of $\lesssim 50\mu rad$, is indispensable for satellite experiments. This mount has to achieve this accuracy with an additional load of 40kg, which is roughly the total weight of the equipment used.

The second Bob is still waiting for his new detectors. When those are available, one can perform measurements with the OGS in Graz and a retro reflecting satellite.

Acknowledgements

Above all, I would like to thank my parents Anneliese and Walter for supporting me all the time without asking me when I'll finally finish.

At this point I would like to express my particular thanks to Prof. Anton Zeilinger, who made Vienna to a hot spot for quantum research and offered me the opportunity to work on this impressive project.

Thanks to my supervisor Dr. Rupert Ursin who gave me a place within this distinguished working group and always pushed me in the right direction.

Without the discussions with Dr. Thomas Scheidl and his help in the laboratory I would have grasped only a fraction of this content.

Thanks Johannes Handsteiner, it is always inspiring and great fun to work with you.

Roland Blach without you this telescope would have never worked.

Thanks to DI Thomas Herbst for the great meals during the time on Roque de los Muchachos and the lift when my tank was empty.

Thanks to DI Bernhard Wittmann for rescuing me from the roof in the middle of the night.

Nina Fleischmann and Ana Rodriguez Aramendia thank you for being great umpa lumpas.

Thanks to my flatmate Alois Wollersberger, for reminding me when its time to stop working and for correcting my terrible mistakes within this thesis.

Thanks to my siblings and friends who were listening to me in times when I was talking about nothing else then my thesis.

Further, I want to thank you, Edith Ober, for giving me the time to write this thesis and all your love.

This work was made possible by grants from the Federal Ministry of Science, Research and Economy(BMWFW) under project QUESS MM725002 and the Austrian Science Foundation(FWF) under project SFB F4008

Appendix A

AIT Detectors

QD800-pQI ▶ Single Photon Detection Module

Description

AIT developed the QD800 pQI series of Single Photon Counting Modules to offer a unique combination of low dark count rates and very low jitter in a miniature package. The special mechanical design allows a flexible combination with existing systems in the laboratory. Incoming photons generate corresponding electrical pulses which may be conveniently read out at the digital output.

Features

- Low dark rates
- Very low jitter
- High detection efficiency (400nm to 1000nm)
- digital output pulse (0,4V) at SMA connector
- Single 5 V DC supply operation
- 42x42 mm (wxh) package suitable with „multicube"

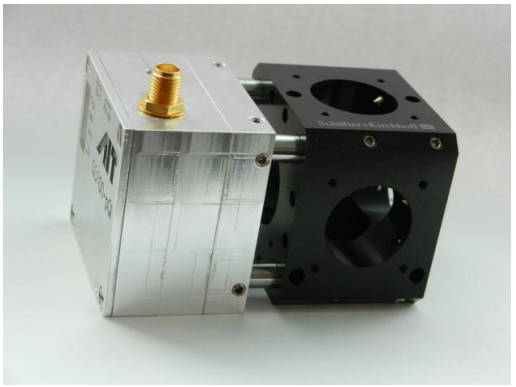

Applications

- Quantum optics, quantum cryptography
- Fiber optics characterization
- Time Correlated Single Photon Counting (TCSPC)
- Fluorescence, fluorescence life time spectroscopy, Raman spectroscopy
- Single photon source characterization
- Eye-safe laser ranging (lidar)
- Time-of-flight measurements (ranging)
- Time-resolved fluorescence spectroscopy
- Fluorescence Lifetime Imaging (FLIM)
- Fluorescence Correlation Spectroscopy (FCS)
- Fluorescence Lifetime Correlation Spectroscopy (FLCS)
- Single molecule spectroscopy
- Optical Time Domain Reflectometry (OTDR)
- Optical tomography

AIT Austrian Institute of Technology GmbH – Safety & Security Department – Donau City Str. 1, 1220 Vienna, Austria

QD800-pQI ▶ Single Photon Detection Module

Technical Specifications

Parameter	Min	Typ	Max	Unit
Spectral range	400		1000	nm
Dark count rate		200		Counts/s
Photon detection efficiency		50		%
Timing resolution		100		ps
Afterpulsing probability		1		%
Dead time range		10		us
Output pulse amplitude (into 50 Ohm)		0,4		V
Digital out – T-OK *)	0		3,3	V
Analog out –Temp **)	0		1,5	V
Supply voltage	4,8	5	5,2	V
Supply current		230		mA
Current for cooling (-20°C at 25°C T_{amb})		110		mA
Current for high voltage (~200V)		20		mA
Current for signal processing and contol		100		mA

*) If the temperature reaches the set point, T-OK goes high.
**) The voltage of the analog out Temp represents the temperature of the SPAD. See diagram below.

Absolute Maximum Ratings

	Min	Typ	Max	Unit
Supply voltage	4	5	5,2	V
Operating temperature	0		40	°C
Storage temperature	-20		70	°C
Count rate			10	MCounts/s

DI Dr. Martin Stierle
+43 (0)50550-4166
+43 (0)664 / 235 18 47
martin.stierle@ait.ac.at

AIT Austrian Institute of Technology GmbH
Safety & Security Department
Donau-City-Str. 1
1220 Wien

DI Gerhard Humer
+43 (0)50550-4128
+43 (0)664 / 620 76 46
gerhard.humer@ait.ac.at

QD800-pQI ▶ Single Photon Detection Module

Temperature diagram

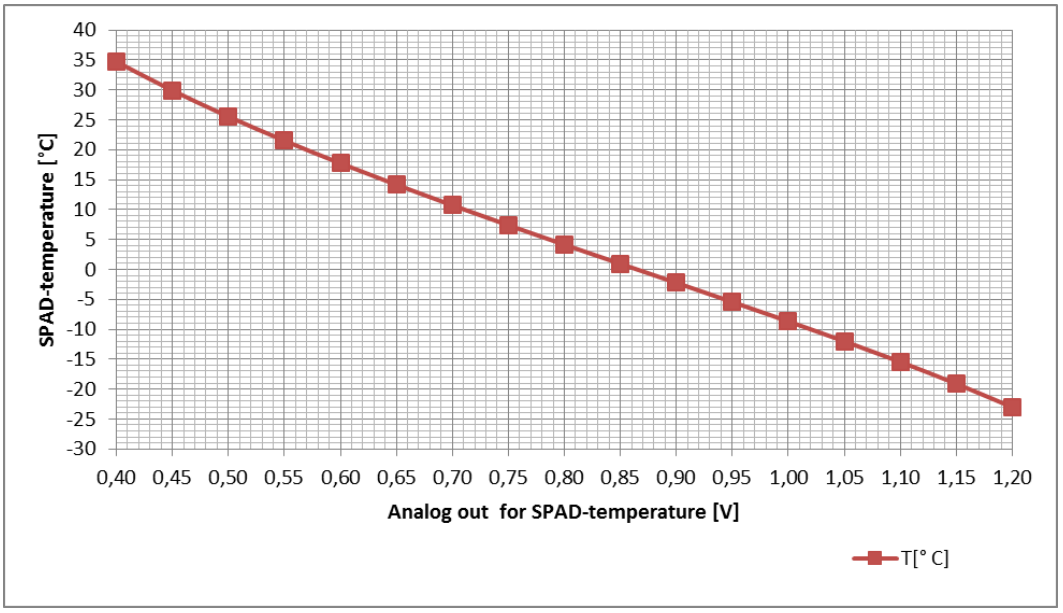

Formula:
T[°C] = 3200/ln((U[V]*89877 / (1,5 - U[V]) - 273,15

Package Drawings

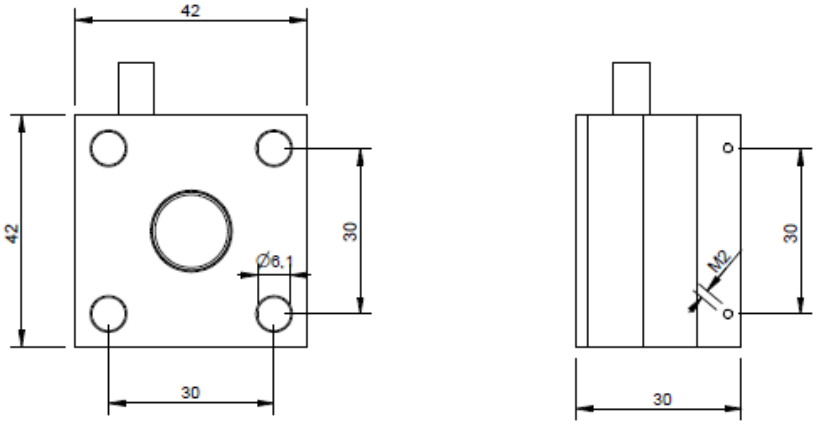

Bibliography

[1] Nicolas Gisin, Grégoire Ribordy, Wolfgang Tittel, and Hugo Zbinden. Quantum cryptography. *Reviews of Modern Physics*, 74(1):145–195, March 2002. doi: 10.1103/RevModPhys.74.145. URL http://link.aps.org/doi/10.1103/RevModPhys.74.145.

[2] D. Stucki, N. Gisin, O. Guinnard, G. Ribordy, and H. Zbinden. Quantum key distribution over 67 km with a plug&play system. *New Journal of Physics*, 4(1): 41, July 2002. ISSN 1367-2630. doi: 10.1088/1367-2630/4/1/341. URL http://iopscience.iop.org/1367-2630/4/1/341.

[3] A. Poppe, A. Fedrizzi, R. Ursin, H. Böhm, T. Lörunser, O. Maurhardt, M. Peev, M. Suda, C. Kurtsiefer, H. Weinfurter, T. Jennewein, and A. Zeilinger. Practical quantum key distribution with polarization entangled photons. *Optics Express*, 12 (16):3865–3871, August 2004. doi: 10.1364/OPEX.12.003865. URL http://www.opticsexpress.org/abstract.cfm?URI=oe-12-16-3865.

[4] Zhiliang Yuan and A. Shields. Continuous operation of a one-way quantum key distribution system over installed telecom fibre. *Optics Express*, 13(2):660–665, January 2005. doi: 10.1364/OPEX.13.000660. URL http://www.opticsexpress.org/abstract.cfm?URI=oe-13-2-660.

[5] Yi Zhao, Bing Qi, Xiongfeng Ma, Hoi-Kwong Lo, and Li Qian. Experimental quantum key distribution with decoy states. *Physical Review Letters*, 96(7):070502, February 2006. doi: 10.1103/PhysRevLett.96.070502. URL http://link.aps.org/doi/10.1103/PhysRevLett.96.070502.

[6] Z. L. Yuan, A. W. Sharpe, and A. J. Shields. Unconditionally secure one-way quantum key distribution using decoy pulses. *Applied Physics Letters*, 90(1):011118, January 2007. ISSN 0003-6951, 1077-3118. doi: 10.1063/1.2430685. URL http://scitation.aip.org/content/aip/journal/apl/90/1/10.1063/1.2430685.

[7] C. Gobby, Z. L. Yuan, and A. J. Shields. Quantum key distribution over 122 km of standard telecom fiber. *Applied Physics Letters*, 84(19):3762–3764, May 2004. ISSN

0003-6951, 1077-3118. doi: 10.1063/1.1738173. URL http://scitation.aip.org/content/aip/journal/apl/84/19/10.1063/1.1738173.

[8] P. A. Hiskett, D. Rosenberg, C. G. Peterson, R. J. Hughes, S. Nam, A. E. Lita, A. J. Miller, and J. E. Nordholt. Long-distance quantum key distribution in optical fibre. *New Journal of Physics*, 8(9):193, September 2006. ISSN 1367-2630. doi: 10.1088/1367-2630/8/9/193. URL http://iopscience.iop.org/1367-2630/8/9/193.

[9] Cheng-Zhi Peng, Jun Zhang, Dong Yang, Wei-Bo Gao, Huai-Xin Ma, Hao Yin, He-Ping Zeng, Tao Yang, Xiang-Bin Wang, and Jian-Wei Pan. Experimental long-distance decoy-state quantum key distribution based on polarization encoding. *Physical Review Letters*, 98(1):010505, January 2007. doi: 10.1103/PhysRevLett.98.010505. URL http://link.aps.org/doi/10.1103/PhysRevLett.98.010505.

[10] Danna Rosenberg, Jim W. Harrington, Patrick R. Rice, Philip A. Hiskett, Charles G. Peterson, Richard J. Hughes, Adriana E. Lita, Sae Woo Nam, and Jane E. Nordholt. Long-distance decoy-state quantum key distribution in optical fiber. *Physical Review Letters*, 98(1):010503, January 2007. doi: 10.1103/PhysRevLett.98.010503. URL http://link.aps.org/doi/10.1103/PhysRevLett.98.010503.

[11] Hiroki Takesue, Sae Woo Nam, Qiang Zhang, Robert H. Hadfield, Toshimori Honjo, Kiyoshi Tamaki, and Yoshihisa Yamamoto. Quantum key distribution over a 40-dB channel loss using superconducting single-photon detectors. *Nature Photonics*, 1(6):343–348, June 2007. ISSN 1749-4885. doi: 10.1038/nphoton.2007.75. URL http://www.nature.com/nphoton/journal/v1/n6/abs/nphoton.2007.75.html.

[12] R. Ursin, F. Tiefenbacher, T. Schmitt-Manderbach, H. Weier, T. Scheidl, M. Lindenthal, B. Blauensteiner, T. Jennewein, J. Perdigues, P. Trojek, B. Ömer, M. Fürst, M. Meyenburg, J. Rarity, Z. Sodnik, C. Barbieri, H. Weinfurter, and A. Zeilinger. Entanglement-based quantum communication over 144 km. *Nature Physics*, 3(7):481–486, July 2007. ISSN 1745-2473. doi: 10.1038/nphys629. URL http://www.nature.com/nphys/journal/v3/n7/abs/nphys629.html.

[13] Tobias Schmitt-Manderbach, Henning Weier, Martin Fürst, Rupert Ursin, Felix Tiefenbacher, Thomas Scheidl, Josep Perdigues, Zoran Sodnik, Christian Kurtsiefer, John G. Rarity, Anton Zeilinger, and Harald Weinfurter. Experimental demonstration of free-space decoy-state quantum key distribution over 144 km. *Physical Review Letters*, 98(1):010504, January 2007. doi: 10.1103/PhysRevLett.98.010504. URL http://link.aps.org/doi/10.1103/PhysRevLett.98.010504.

[14] Alessandro Fedrizzi, Rupert Ursin, Thomas Herbst, Matteo Nespoli, Robert Prevedel, Thomas Scheidl, Felix Tiefenbacher, Thomas Jennewein, and Anton

Zeilinger. High-fidelity transmission of entanglement over a high-loss freespace channel. *Nature Physics*, 5(6):389–392, June 2009. ISSN 1745-2473, 1745-2481. doi: 10.1038/nphys1255. URL http://arxiv.org/abs/0902.2015. arXiv:0902.2015 [quant-ph].

[15] Thomas Herbst, Thomas Scheidl, Matthias Fink, Johannes Handsteiner, Bernhard Wittmann, Rupert Ursin, and Anton Zeilinger. Teleportation of entanglement over 143 km. *arXiv:1403.0009 [physics, physics:quant-ph]*, February 2014. URL http://arxiv.org/abs/1403.0009.

[16] A. Einstein, B. Podolsky, and N. Rosen. Can quantum-mechanical description of physical reality be considered complete? *Physical Review*, 47(10):777–780, May 1935. doi: 10.1103/PhysRev.47.777. URL http://link.aps.org/doi/10.1103/PhysRev.47.777.

[17] JOHN S. BELL. On the problem of hidden variables in quantum mechanics. *Reviews of Modern Physics*, 38(3):447–452, July 1966. doi: 10.1103/RevModPhys.38.447. URL http://link.aps.org/doi/10.1103/RevModPhys.38.447.

[18] John F. Clauser, Michael A. Horne, Abner Shimony, and Richard A. Holt. Proposed experiment to test local hidden-variable theories. *Physical Review Letters*, 23(15): 880–884, October 1969. doi: 10.1103/PhysRevLett.23.880. URL http://link.aps.org/doi/10.1103/PhysRevLett.23.880.

[19] Marc Jofre, Arnaud Gardelein, Gabriele Anzolin, Waldimar A. Amaya, Jose Capmany, Rupert Ursin, L. Peñate, D. Lopez, José Luis San Juan, J. A. Carrasco, F. Garcia, Francisco Jose Torcal-Milla, Luis Miguel Sanchez-Brea, Eusebio Bernabeu, Josep Perdigues, Thomas Jennewein, J P Torres, M. W. Mitchell, and Valerio Pruneri. Fast optical source for quantum key distribution based on semiconductor optical amplifiers. *Optics Express*, 19(5):3825–3834, 2011. doi: 10.1364/OE.19.003825.

[20] Max Born and Emil Wolf. *Principles of Optics*. URL https://archive.org/stream/PrinciplesOfOptics/BornWolf-PrinciplesOfOptics#page/n431/mode/2up.

[21] A. Kolmogorov. The local structure of turbulence in incompressible viscous fluid for very large reynolds' numbers. *Akademiia Nauk SSSR Doklady*, 30:301–305, 1941. ISSN 0002-3264. URL http://adsabs.harvard.edu/abs/1941DoSSR..30..301K.

[22] Larry C. Andrews. *Field Guide to Atmospheric Optics*. SPIE, 1000 20th Street, Bellingham, WA 98227-0010 USA, January 2004. ISBN 9780819453181. URL http://ebooks.spiedigitallibrary.org/book.aspx?bookid=148.

[23] D. L. FRIED. Optical resolution through a randomly inhomogeneous medium for very long and very short exposures. *Journal of the Optical Society of America*, 56 (10):1372–1379, October 1966. doi: 10.1364/JOSA.56.001372. URL http://www.opticsinfobase.org/abstract.cfm?URI=josa-56-10-1372.

[24] Tobias Schmitt-Manderbach. *Long distance free-space quantum key distribution*. PhD thesis, Ludwig–Maximilians–Universit, München, October 2007. URL http://edoc.ub.uni-muenchen.de/8102/1/Schmitt-Manderbach_Tobias.pdf.

[25] Larry C. Andrews and Ronald L. Phillips. *Laser Beam Propagation Through Random Media*. SPIE Press, January 2005. ISBN 9780819459480.

[26] Wolfgang Demtröder. *Experimentalphysik 2: Elektrizität und Optik*. Springer, Berlin; Heidelberg; New York, auflage: 5., überarb. u. erw. aufl. 2009 edition, December 2008. ISBN 9783540682103.

[27] X. Baillard, A. Gauguet, S. Bize, P. Lemonde, Ph Laurent, A. Clairon, and P. Rosenbusch. Interference-filter-stabilized external-cavity diode lasers. *Optics Communications*, 266(2):609–613, October 2006. ISSN 00304018. doi: 10.1016/j.optcom.2006.05.011. URL http://arxiv.org/abs/physics/0605046. arXiv:physics/0605046.

[28] P. H. LISSBERGER and W. L. WILCOCK. Properties of all-dielectric interference filters. II. filters in parallel beams of light incident obliquely and in convergent beams. *Journal of the Optical Society of America*, 49(2):126–128, February 1959. doi: 10.1364/JOSA.49.000126. URL http://www.opticsinfobase.org/abstract.cfm?URI=josa-49-2-126.

[29] S. Cova, M. Ghioni, A. Lacaita, C. Samori, and F. Zappa. Avalanche photodiodes and quenching circuits for single-photon detection. *Applied Optics*, 35(12): 1956–1976, April 1996. doi: 10.1364/AO.35.001956. URL http://ao.osa.org/abstract.cfm?URI=ao-35-12-1956.

[30] Mario Stipcevic, Daqing Wang, and Rupert Ursin. Characterization of a commercially available large area, high detection efficiency single-photon avalanche diode. *Journal of Lightwave Technology*, 31(23):3591–3596, December 2013. URL http://jlt.osa.org/abstract.cfm?URI=jlt-31-23-3591.

[31] Roger Newman. Visible light from a silicon p-n junction. *Physical Review*, 100(2): 700–703, October 1955. doi: 10.1103/PhysRev.100.700. URL http://link.aps.org/doi/10.1103/PhysRev.100.700.

[32] Richard D. Younger, K. Alex McIntosh, Joseph W. Chludzinski, Douglas C. Oakley, Leonard J. Mahoney, Joseph E. Funk, Joseph P. Donnelly, and S. Verghese.

Crosstalk analysis of integrated geiger-mode avalanche photodiode focal plane arrays</title>. pages 73200Q–73200Q–12, May 2009. doi: 10.1117/12.819173. URL http://dspace.mit.edu/handle/1721.1/52684.

[33] Cristian Bonato, Markus Aspelmeyer, Thomas Jennewein, Claudio Pernechele, Paolo Villoresi, and Anton Zeilinger. Influence of satellite motion on polarization qubits in a space-earth quantum communication link. *Optics Express*, 14(21):10050–10059, October 2006. doi: 10.1364/OE.14.010050. URL http://www.opticsexpress.org/abstract.cfm?URI=oe-14-21-10050.